Adaptive Disturbance-Based High-Order Sliding Mode Control for Hypersonic Entry Vehicles

Marco Sagliano[1]
Deutsches Zentrum für Luft- und Raumfahrt, Bremen, Germany, 28359

Erwin Mooij[2]
Delft University of Technology, Delft, The Netherlands, 2629

Stephan Theil[3]
Deutsches Zentrum für Luft- und Raumfahrt, Bremen, Germany, 28359

In this paper an adaptive, disturbance-based sliding-mode controller for hypersonic entry vehicles is proposed. The scheme is based on high-order sliding-mode theory, and is coupled to an extended sliding-mode observer, able to reconstruct online the disturbances. The result is a numerically-stable control scheme, able to adapt online to reduce the error in presence of multiple uncertainties. The transformation of a high-order sliding-mode technique into an adaptive law by using the extended sliding-mode observer is, together with the multi-input, multi-output formulation for hypersonic entry vehicles, the main contribution of this paper. The robustness is verified with respect to perturbations in terms of initial conditions, atmospheric density variations, as well as mass and aerodynamic uncertainties. Results show that the approach is valid, leading to accurate disturbance reconstruction, to a better transient, and to good tracking performance, improved of about 50% in terms of altitude and range errors with respect to the corresponding standard sliding-mode control approach.

---

[1] GNC Engineer, Navigation and Control Department, AIAA Member
[2] Assistant Professor, Astrodynamics and Space Missions Department, Faculty of Aerospace Engineering, AIAA Associate Fellow
[3] GNC Department Head, Guidance, Navigation and Control Department

Nomenclature

Roman

$a(\mathbf{x}), b(\mathbf{x})$ = Generic functions

a_h = Third time derivative of h not dependent on control, (m/s^3)

a_V = Second time derivative of V not dependent on control, (m/s^3)

$b_{h,\alpha}$ = Third time derivative of h dependent on u_α, (m/s^2)

$b_{h,\mu}$ = Third time derivative of h dependent on u_σ, (m/s^2)

$b_{V,\alpha}$ = Second time derivative of V dependent on u_α, (m/s^2)

$b_{V,\mu}$ = Second time derivative of V dependent on u_μ, (m/s^2)

C_D = Drag coefficient

C_L = Lift coefficient

d = Generic unknown function

d_h = Altitude-related disturbance / uncertainty, (m/s^3)

d_V = Velocity-related disturbance / uncertainty, (m/s^3)

g = gravitational acceleration, (m/s^2)

h = Altitude, (m)

k_i = Nonlinear sliding-mode gains of the i^{th} variable

L = lift acceleration, (m/s^2)

M = Mach number

n_z = Load factor

$\bar{q}$ = Dynamic pressure, (N/m^2)

$\dot{Q}$ = Heat flux, (W/m^2)

r = Radial position, (m)

r_D = Relative degree of the system

R_{gas} = Specific gas constant, (J/(kg K))

T = Temperature, (K)

T_h = Temperature derivative with respect to the altitude, (K/m)

u_α = feedback angle-of-attack rate, (rad/s)

u_μ = feedback bank-angle rate, (rad/s)

V = Velocity modulus, (m/s)

$\mathbf{x}(t)$ = State vector

Greek

α = Angle of attack, (rad)

μ = Bank angle, (rad)

γ = Flight-path angle, (rad)

γ_{gas} = Specific heat ratio

ϕ = Latitude, (rad)

λ_i^m = i^{th} Linear sliding-mode gains of the k^{th} variable

κ_i^m = i^{th} Nonlinear sliding-mode gains of the k^{th} variable

ψ = Velocity azimuth angle, (rad)

ρ = Atmospheric density, (kg/m^3)

σ = Generic sliding variable

σ = Standard deviation

θ = Longitude, (rad)

Operators

$\dot{(\cdot)}$ = First time derivative, $((\cdot)\ /s)$

$\ddot{(\cdot)}$ = Second time derivative, $((\cdot)\ /s^2)$

$\dddot{(\cdot)}$ = Third time derivative, $((\cdot)\ /s^3)$

$\widehat{(\cdot)}$ = Estimate of $(\cdot)$, $(\cdot)$

$\tilde{(\cdot)}$ = Residual of $(\cdot)$, $(\cdot)$

sgn = sign function

sat = saturation function

$(\cdot)_{(\cdot)}$ = Generic subscript

$(\cdot)_{ref}$ = Reference variable

I. Introduction

Entry guidance of an unpowered vehicle is a difficult task, as the problem is governed by nonlinear equations of motion, and multiple constraints acting on the vehicle must be taken into account. For this reason, decades of research have provided several methods for dealing with this problem. Among these, the so-called Apollo entry guidance [1] has gained popularity in terms of reliability, and has been used since the beginning of the Apollo program itself until the last NASA missions, e.g., the Mars Science Laboratory [2, 3]. This method is based on the design of one or more reference drag-velocity (or, alternatively, drag-energy) profiles that satisfy the requirements of the mission. In the hypothesis of having a nominal angle of attack, it is possible to extract the longitudinal states, that is, the altitude, the velocity, and the flight-path angle, as well as the bank-angle command from the drag-energy model. Lateral motion is usually controlled with so-called bank reversals, consisting of a rapid change of the sign of the bank angle, but preserving its modulus. With this approach it is possible to keep the heading-alignment error under control, while minimizing the impact of the lateral guidance on the longitudinal performance of the system.

Over the last years, an alternative to the class of drag-energy methods has arisen, based on the use of optimal control theory, and several tools have been developed over the years, such as DIDO [4, 5] and SPARTAN [6, 7]. The problem is described in terms of a cost function to be minimized (or maximized) and the differential equations representing the motion of the vehicle. Moreover, other constraints, such as the load factor and the heat-flux, can be included in the optimization problem as nonlinear algebraic constraints. The optimal-control problem can be transcribed and solved with one of the many off-the-shelf available software, e.g. SNOPT [8] or IPOPT [9].

These two families of methods rely on several assumptions, though. For instance, they use analytical or semi-analytical models for the gravity field and the atmospheric density. Moreover, dispersions on the initial states, the mass of the vehicle and other external disturbances affect the performance of the system. Therefore a feedback scheme, able to track the desired trajectory and to reject these disturbances, is required. On this subject several alternatives have been proposed over the years. In [10] and [11] linear and nonlinear feedback laws with a proportional-integral-derivative (PID) structure for the longitudinal tracking was proposed. The lateral error was in both cases kept

under control with the bank-reversal management logic.

Alternatively, in [12] and [13] the use of different tracking laws based on a trade-off between longitudinal and lateral guidance performance were suggested, while in [14] a pre-TAEM (terminal area for energy management) ground-track control to limit the heading error was adopted. Other possible solutions foresaw the use of a receding-horizon scheme based on the linearized time-varying dynamics to be controlled [15], and a unified predictor-corrector algorithm [16], which covers all the possible entry mission profiles. The problem was also approached by using different gain-scheduling controllers [17, 18], or by tracking altitude and velocity via Model Reference Adaptive Control (MRAC) [19, 20]. A possible alternative to the state-tracking schemes is a generalized constraint-tracking guidance, with a particular emphasis on the tracking of the heat-flux [21, 22].

A different way to approach the tracking problem comes from the field of attitude-control techniques, more specifically sliding mode control (SMC) [23], which shows excellent robustness against perturbations with known upper bounds. This technique can be applied to nonlinear systems, therefore no large amount of information has to be stored, as is the case for H_∞ controllers, which suffer from the rapid increase of the number of states needed to represent the uncertainties, and the need to apply a gain-scheduling technique, since they are conceived for linear systems.

Another advantage associated with the use of SMC techniques is its robustness with respect to uncertainties and disturbances, because of its nonlinear nature. Interesting results for the entry problem have been obtained by using terminal-guidance High-Order Sliding Mode (HOSM) controllers, in both the time [24] and the range [25] domain, respectively. They are based on the definition of sliding surfaces associated with predefined terminal conditions to be achieved. More recently, a new class of adaptive high-order sliding-mode controllers was proposed [26–28]. These methods generalize the possibility to apply virtually chattering-free sliding-mode controllers to systems with relative degree larger than one [29]. The controller is made adaptive by using a a double-layer strategy to estimate online the minimum gain required to dominate unknown, but bounded disturbances acting on the system. The adaptation is obtained by using the concept of equivalent control, filtered out from the current control signal, and fed-back into the double-layer algorithm. However, a drawback of this technique is the small step-size required to obtain a stable numerical scheme for the gains.

Moreover, it requires the design of a dedicated differentiator, which represents a parasitic dynamics [30], and needs to be included in the loop.

In this work an alternative adaptive disturbance-based high-order sliding-mode control (AD-HOSMC) scheme, based on an extended sliding mode observer (SMO), is proposed. Instead of estimating the equivalent control via low-pass filtering, we propose to use a multi-input, multi-output (MIMO) sliding-mode disturbance observer, able to reconstruct online the disturbances acting on the system, and at the same time, to observe the σ-dynamics, that is, the sliding variables representing the state errors, which can be fed in the loop. The advantage of this approach is twofold. First, it relaxes the requirements for the step-size needed for the scheme. Second, at the same time it provides the derivatives of the sliding variables needed to compute the tracking law.

The vehicle considered in this paper is the SHEFEX-3 (SHarp Edge Flight EXperiment) prototype, a vehicle planned by the German Aerospace Center (DLR) [31, 32] for the demonstration of several entry technologies. The proposed tracking law can be used as feedback control scheme together with onboard trajectory-generation algorithms [33, 34], as well as in conjunction with pure optimal trajectory-generation tools [6, 7]. The work is organized as follows. In Sec. II the vehicle and the scenario are briefly introduced, while in Sec. III the adaptive high-order sliding-mode is described in detail, together with a series of simulations coming from a simplified example motivating the current work. In Sec. IV the proposed technique is applied to the longitudinal equations of motion of an unpowered entry vehicle, while Sec. V focuses on the validation of the proposed algorithms, and compares the results with a traditional sliding-mode control algorithm. Finally, in Sec. VI some conclusions on the work are drawn.

II. Vehicle and Scenario Characterization

SHEFEX is a program of technological development for atmospheric entry, conceived and led by the German Aerospace Center over the last 20 years [35]. The idea is to test technologies for atmospheric entry, such as structural and thermal-protection systems, with the focus to transform blunt areas into flat surfaces, to reduce costs without penalizing system performance.

SHEFEX-1 was successfully launched on October 27, 2005 from Andøya Rocket Range in An-

denes, Norway. The experiments measured several aerodynamics parameters, and their effect on the structure during atmospheric entry, and used passive control during entry. This mission also demonstrated that sounding rockets are suitable for atmospheric entry experiments. The SHEFEX project served as a starting point for SHEFEX-2, launched on June 22, 2012 also from Andøya Rocket Range. The goal of SHEFEX-2 was to validate analytical predictions and ground-test data, and to investigate technologies for hypersonic and space-transportation systems. To go on with the effort to increase the technological level for real space missions, the development of SHEFEX-3 began in 2012. The SHEFEX-3 vehicle has a faceted surface, which guarantees minor costs in terms of manufacturing. One of the proposed designs (the reference one for this work) is shown in Fig. 1.

Fig. 1 SHEFEX-3 Entry vehicle.

The reference surface is equal to 0.468 m^2. The vehicle has its center of mass (CoM) at 55%, starting from the nose, and is fully trimmable.

Table 1 SHEFEX-3 vehicle parameters and initial state.

Parameter	Value	Unit	State	Initial Value	Unit
mass	500	kg	Altitude h	100.0	km
reference surface	0.468	m^2	Longitude θ	2.1	deg
length	1.85	m	Latitude ϕ	68.5	deg
width	1.85	m	Velocity modulus V	6500.0	m/s
height	0.66	m	Flight-path angle γ	0.0	deg
CoM	55%	-	Heading angle γ	-144.0	deg

The entry interface has an initial altitude and velocity of 100 km and 6.5 km/s, respectively, and an initial flight-path angle is equal to 0. Details on the entry interface and the vehicle data are listed in Table 1, while the open-loop results are presented in Figs. 2-3. The open-loop commands are defined as follows: the angle of attack is initially equal to 45 deg, and slowly decreases until the value of 22 deg (corresponding to the max L/D) is achieved. This guarantees the correct exposure of the thermal-protection system at the beginning of the mission, when a large heat-flux is experienced, while in the second part of the mission the L/D ratio is maximized to extend the range capabilities of the vehicle. The bank-angle profile varies from an initial value of 60 deg to a value of 45 deg to ensure a sufficient margin of controllability.

The reference controls ensure proper final conditions in terms of altitude and velocity, which allow for the opening of the parachute system, while providing sufficient range, required for the onboard experiments. It is worth mentioning that angular-rate limits were included in the design of the control strategy. Specifically, these limits are equal to 5 deg/s for both the angle-of-attack rate and the bank-angle rate, and are compatible with the constraints coming from the flight-control system. In the frame of this work no lateral control is included. However, the method can be fully coupled with bank-reversal management, or with other lateral control schemes.

Figure 2 shows the open-loop trajectory. Specifically, the plots in the top-left and the center-left, representing the altitude (Fig. 2(a)) and the flight-path angle (Fig. 2(c)), show one of the difficulties associated with this scenario, i.e., the phugoid oscillations (typycal of flight at max L/D), and a high-variability of the states, which require an adequate reaction capability of the control scheme to be employed. In Fig. 2(b) the velocity modulus is depicted, where one can see that the velocity is almost constant during the first 200 s (as the drag is too low to reduce it), and then decreases once that the vehicle experiences a thicker atmospheric density, and therefore, a larger drag acceleration. In Fig. 2(d) plot the nominal range is depicted. One can see that the spacecraft travels for about 3,000 km. Plots in Figs. 2(e) and 2(f) present the corresponding open-loop profiles of angle of attack and bank angle.

Finally, in Fig. 3 the constraints acting on the vehicle, i.e., the dynamic pressure $\overline{q}$ (Fig. 3(a)), the heat flux $\dot{Q}$ (Fig. 3(b)), and the vertical load factor n_z (Fig. 3(c)), together with their

corresponding limits, are depicted. Specifically, they are computed as

$$\bar{q} = \tfrac{1}{2}\rho V^2, \;\; \dot{Q} = k_q \sqrt{\rho} V^3, \;\; n_z = \tfrac{|L\cos\alpha + D\sin\alpha|}{g_0} \tag{1}$$

where ρ is the atmospheric density, expressed in $\mathrm{kg/m^3}$, k_q is a constant depending on the material and the geometry of the thermal protection system, for SHEFEX-3 equal to $3.111 \cdot 10^{-4}$ $\mathrm{kg^{1/2}/m^3}$, and g_0 is the gravity acceleration at sea level, ($g_0 = 9.806$ $\mathrm{m/s^2}$). The structural limits of the vehicle and the active thermal-protection system dictate a limit for the above constraints. These limits are equal to $\bar{q}_U = 2 \cdot 10^4$ $\mathrm{N/m^2}$, $\dot{Q}_U = 2.5$ $\mathrm{MW/m^2}$, and $n_{z,U} = 5$ g, respectively.

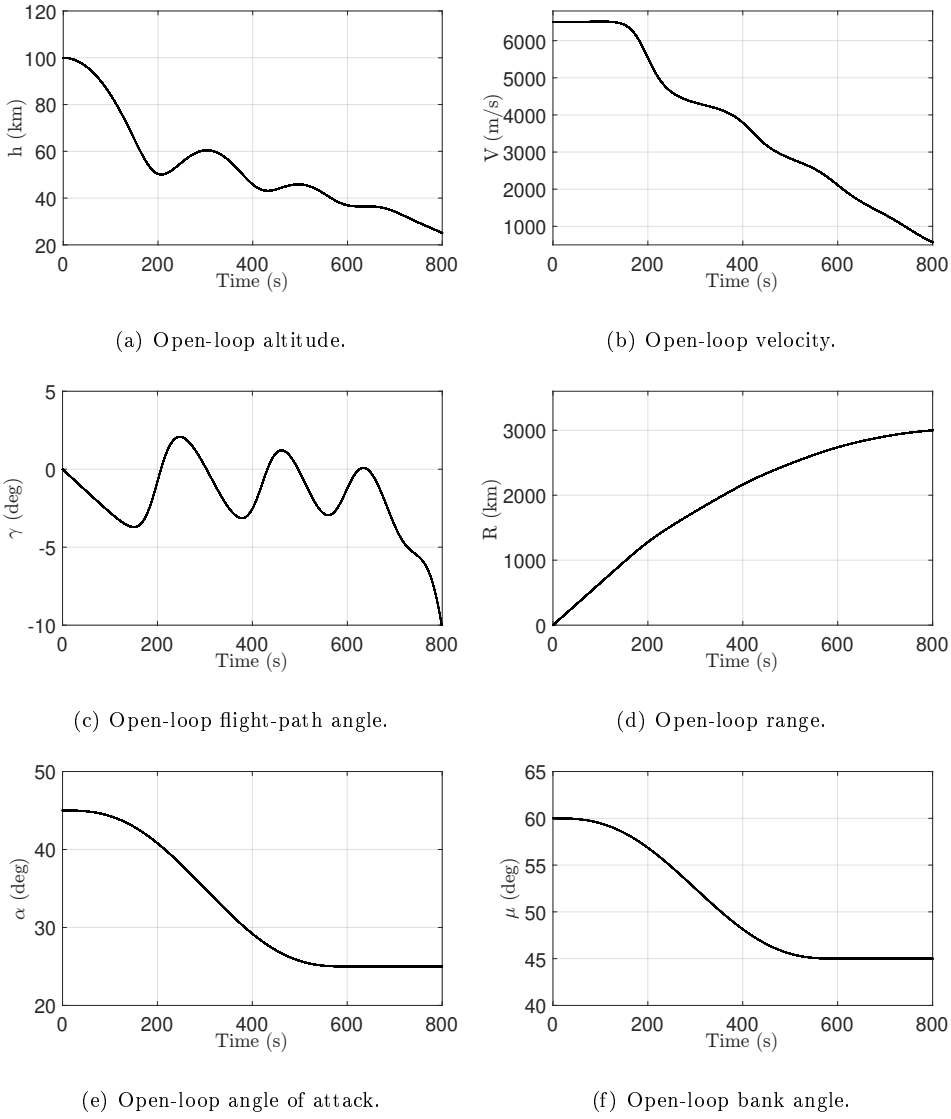

(a) Open-loop altitude.

(b) Open-loop velocity.

(c) Open-loop flight-path angle.

(d) Open-loop range.

(e) Open-loop angle of attack.

(f) Open-loop bank angle.

Fig. 2 Open-loop trajectory - states and controls.

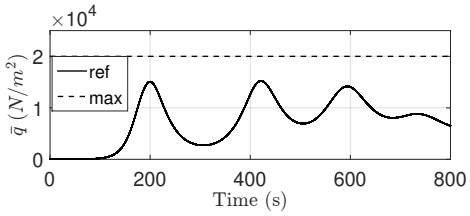

(a) Open-loop dynamic pressure.

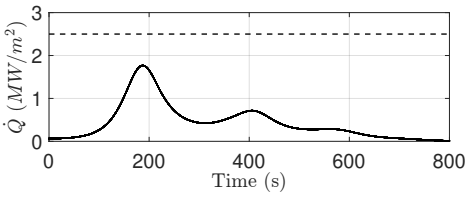

(b) Open-loop heat flux.

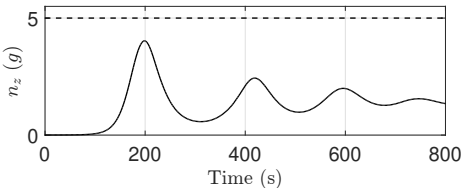

(c) Open-loop load factor.

Fig. 3 Open-loop trajectory - constraints.

III. Adaptive Disturbance-Based High-Order Sliding Mode Control

In this section the adaptive disturbance-based high-order sliding mode control approach is explained. Subsections III.A and III.B describe the high-order sliding-mode theory, and the extended sliding-mode disturbance observer, respectively. Their combination leads to the proposed AD-HOSMC approach. In subsection III.C a practical example, motivating this work, is shown.

A. High-Order Sliding Mode Theory

High-order sliding mode theory deals with the design of robust controllers for nonlinear systems. The name refers to the fact that the system to control is expressed in affine form with respect to the control signals. This is done by differentiating the equations of motion until the control appear linearly. We refer to the n$^{\text{th}}$-order sliding mode controller when the highest derivative of the state to track is of order n. It is therefore possible to link the state errors to the so-called *sliding surfaces*. The control will constrain the system to stay on this sliding surface, and this will ensure the correct tracking of the reference signals. As practical example suppose that we have the system dynamics described by

$$\sigma^{(n)}(t) = a(t) + b(t)u \tag{2}$$

where $\sigma(t) \in \mathbb{R}$ is the state error or equivalently, the sliding variable associated with the state $x(t)$, and defined as $x(t) - x_{\text{ref}}(t)$, $a(t)$ and $b(t)$ are known functions $\in \mathbb{R}$, and $u(t) \in \mathbb{R}$ is the control. In real applications, the functions $a(t)$ and $b(t)$ do not perfectly match the models. Moreover, unmodeled terms may affect the results. We can therefore rewrite Eq. (2) as

$$\sigma^{(n)}(t) = a(t) + \Delta a(t) + (b(t) + \Delta b(t))u = a(t) + b(t)u + d(t) \tag{3}$$

where $d(t) \in \mathbb{R}$ is an unknown, bounded function. Note that the function $d(t)$ may contain combinations of several uncertainties and/or disturbances. That is,

$$d(t) = \Delta a(t) + \Delta b(t)u + d_u(t) \tag{4}$$

with $\Delta a(t)$ and $\Delta b(t)$ representing errors in the models of $a(t)$ and $b(t)$, and $d_u(t)$ includes further, unknown terms. The operator $()^{(n)}$ in Eqs. (2), and (3) represents the n^{th} derivative with respect to the independent variable, in this case the time t.

Proposition 1. Consider Eq. (2) in the nominal case (i.e., $d(t) = 0$). In the hypothesis of $b(t) \neq 0$ it is possible to state that the high-order sliding-mode control

$$\begin{aligned} u &= -b(t)^{-1}\left(\tilde{u} + a(t)\right), \\ \tilde{u} &= \sum_{i=0}^{n-1} \gamma_i \left|\sigma^{(i)}(t)\right|^{\alpha_i} \operatorname{sgn}\left(\sigma^{(i)}(t)\right) \end{aligned} \tag{5}$$

stabilizes the nonlinear system described by Eq. (2) if the terms γ_i are taken such that the polynomial

$$f(p) = p^n + \gamma_n p^{n-1} + \cdots + \gamma_1 \tag{6}$$

is *Hurwitz*, (that is, all its roots have negative real parts), and the terms α_i are computed according to the formula

$$\alpha_{i-1} = \tfrac{\alpha_i \alpha_{i+1}}{2\alpha_{i+1} - \alpha_i}, \;\; i = 2, \ldots, n \tag{7}$$

with $\alpha_{n+1} = 1$, and the seed α_n is defined in the range $[1 - \epsilon, 1)$, with $\epsilon << 1$.

Proof. In [29], Proposition 8.1 it is possible to find a rigorous proof of Proposition 1 for the special case $a(t) = 0$, $b(t) = 1$. If we replace the affine mapping between control u and pseudocontrol $\tilde{u}$ defined as

$$u = -b(t)^{-1}(\tilde{u} + a(t)) \tag{8}$$

in Eq. (4), the system is reduced to

$$\sigma^{(n)}(t) + \sum_{i=0}^{n-1} \gamma_i \left|\sigma^{(i)}(t)\right|^{\alpha_i} \operatorname{sgn}\left(\sigma^{(i)}(t)\right) = 0 \tag{9}$$

For the system described in Eq. (9) Proposition 8.1 of [29] directly holds. The proof is complete, and is valid for the generic case $a(t) \neq 0$, $b(t) \neq 0, 1$.

Remark.1 Note that Eqs. (5) and (8) define a continuous controller. As a consequence, no chattering affects the system, and therefore, no saturation functions need to be selected to mitigate this effect at the expense of a robustness decrease.

The nominal case represented by Eq. (2) is still a special case. In general, there will be disturbances and uncertainties, which will make the $d(t)$ term different from zero. Edwards and Shtessel proposed an adaptive controller, based on a double-layer scheme, able to capture the derivative of the disturbance $\dot{d}(t)$, and to use it to estimate online the gain able to dominate the disturbance $d(t)$ [28]. The scheme works very well for small step-sizes, which are suitable for industrial applications. However, for entry-guidance schemes this approach may be complicated to be used, as outer-loop control-system frequencies are usually lower (in the order of 1-10 Hz), and the aforementioned approach may lead to numerical instabilities. Moreover, the scheme still requires the design of a numerical differentiator, as not all the derivatives of the states (required in Eq. (5)), which are involved in the feedback loop, are directly measured.

Therefore, to guarantee the validity of hypothesis of Proposition 8.1 in [29] also in presence of unknown disturbances we propose an alternative scheme, able to cope with larger step-sizes without reducing the accuracy of the results. The scheme is at the same time able to observe the σ-dynamics by only using measurements of the states, and not their derivatives, and is based on sliding-mode differentiation theory [36, 37].

B. Extended Sliding-Mode Observer

Let us define an augmented σ-state $\sigma_a \in \mathbb{R}^{n+1}$, defined as

$$\sigma_a = \left[\begin{array}{cccc} \sigma_{a,1}, & \ldots, & \sigma_{a,n}, & \sigma_{a,n+1} \end{array} \right]^T \tag{10}$$

where $\sigma_{a,n+1} = d(t)$. The dynamics of Eq. (3) can be rewritten as

$$\begin{aligned} \dot{\sigma}_{a,1} &= \sigma_{a,2} \\ &\vdots \\ \dot{\sigma}_{a,n} &= a + bu + d \\ \dot{\sigma}_{a,n+1} &= \dot{d} \end{aligned} \tag{11}$$

A system in the form of Eq. (11) can be estimated by using the sole measurement of the first state σ_1, supposed to be available [36, 37]; (here the hypothesis of having a pure regulator problem, that is, $x_{1,ref} = 0$, $\sigma_1 = x_1 - x_{1,ref} = x_1$, is implicitly assumed, while the general tracking problem is treated in Sec. IV). The sliding-mode observer can be written as

$$\begin{aligned} \dot{\widehat{\sigma}}_{a,1} &= \widehat{\sigma}_{a,2} + \lambda_1 \tilde{\sigma}_{a,1} + \kappa_1 \operatorname{sgn}(\tilde{\sigma}_{a,1}) \\ &\vdots \\ \dot{\widehat{\sigma}}_{a,n} &= a + bu + \lambda_n \tilde{\sigma}_{a,1} + \kappa_n \operatorname{sgn}(\tilde{\sigma}_{a,1}) \\ \dot{\widehat{\sigma}}_{a,n+1} &= \lambda_{n+1} \tilde{\sigma}_{a,n+1} + \kappa_{n+1} \operatorname{sgn}(\tilde{\sigma}_{a,1}) \end{aligned} \tag{12}$$

where $\tilde{\sigma}_{a,1}$ is defined as $\sigma_1 - \widehat{\sigma}_{a,1}$. The terms $\lambda_i > 0$, $i = [1, n+1]$ are linear gains, chosen such that the dynamics described by Eq. (12) is stable, and defines a Luenberger observer. Nonlinear gains $\kappa_i > 0$, $i = [1, n+1]$ define a sliding-mode behavior, and enforce the variables $\widehat{\sigma}_i$ to converge exponentially to the true sliding states σ_i, $i = [1, n+1]$, within an accuracy defined by a constant ϵ such that

$$\|\sigma_1(t) - \widehat{\sigma}_1(t)\| \ll \epsilon \ll 1 \tag{13}$$

The consequence is that the estimated σ-states converge to the true ones, while the $(n+1)^{\text{th}}$ component converges to the disturbance $d(t)$, which means that the disturbance is reconstructed in real-time, and can be used to make the controller defined in Eq. (5) adaptive.

Proposition 2. The structure defined in Eq. (12) converges to the true σ-state provided that $\kappa_1 > |\sigma_{a,2}(t) - \widehat{\sigma}_{a,2}(t)|_{max}$.

Proof. A formal proof of Proposition 2 is described in [36].

Remark 2. Note that the availability of σ_1 is a realistic hypothesis, as for the case of atmospheric entry, measurements of altitude and velocity, available from the navigation solution, are employed [38].

Remark 3. A more general criterion for the selection of the linear and nonlinear gains, which appear in Eq. (12) is described in Sec. III.C.

If we indicate the estimate of the disturbance $d(t)$ as $\widehat{d}(t)$ we can modify Eq. (5), and define the disturbance-based, high-order sliding mode control law as

$$u = -\widehat{b}^{-1}\left(\tilde{u} + \widehat{a} + \widehat{d}\right), \qquad \tilde{u} = \sum_{i=0}^{n-1} \gamma_i \left|\sigma^{(i)}\right|^{\alpha_i} \operatorname{sgn}\left(\sigma^{(i)}\right) \tag{14}$$

where $\widehat{a}$ and $\widehat{b}$ are the nominal functions a and b computed by using the states estimates and obtained by the sliding-mode observer; this online estimator also provides the disturbance estimate $\widehat{d}$.

Proposition 3. Suppose that the disturbance signal $d(t)$ is bounded, together with its first and second derivatives, that is, there exist some values δ_0, δ_1, δ_2 such that $|d(t)| \leq \delta_0$, $\left|\dot{d}(t)\right| \leq \delta_1$ and $\left|\ddot{d}(t)\right| \leq \delta_2$. Then the adaptive law defined by Eq. (14) drives the dynamics of Eq. (5) towards the equilibrium point $[\sigma_1, \ldots, \sigma_n]^T = [0, \ldots, 0]^T$ in finite time.

Proof Let us assume that the conditions for the sliding-mode observer existence hold. Then, each of the variables in the sliding-mode observer of Eq. (11) will converge to the true ones, as stated in **Proposition 2**. This means that once the observation sliding surface $\sigma_{a,1}$ is reached and maintained, the dynamics is reduced to Eq. (9), and Proposition 8.1 of [29] once again holds. The proof is complete.

Remark 4. Note that this is a theoretical result. In practice, what we obtain by using the adaptive law of Eq. (14) is a dramatic reduction of the disturbance acting on the system from the full unknown disturbance term d to a much smaller residual $\epsilon_d = d - \widehat{d}$, which is bounded, by

$$|\epsilon_d| < \frac{\epsilon_0}{\mu} \tag{15}$$

where $\epsilon_0 \ll 1$ is a tuning parameter in the sliding-mode observer, and μ is the eigenvalue of the observer, properly defined in Sec. V.B, and taken ≥ 1 throughout this work. However, given the robustness of the HOSM framework, and the exponential stability of the nonlinear observer, the convergence is fast, and the proposed adaptive law makes the controller able to work in quasi-ideal conditions.

IV. A Motivational Example

In this subsection a simple example illustrating the motivation of the work is described. Suppose we have a system of third-order, defined as

$$\sigma^{(3)}(t) = a(t) + b(t)u + d(t) \tag{16}$$

where a and b are equal to 2 and 4, respectively, while $d(t)$ is a time-dependent uncertainty acting on the system. Suppose that the initial state is defined as $\sigma = [1 \;\; 0.5 \;\; 0]^T$, and that, in absence of uncertainties (i.e, $d(t) = 0$) we apply the controller defined by Eq. (5). Results are omitted for brevity, but one can observe some of the interesting features of HOSM theory: the error converges to the equilibrium point $[0, \;\; 0, \;\; 0]^T$ in finite time, and the control signal does not show any trace of the chattering phenomenon. Let us consider the presence of the disturbance $d(t)$. A possible approach to take the (unknown) disturbance $d(t)$ into account is to define a double-layer adaptive scheme, based on the use of the so-called *equivalent control* [27, 28, 30]. The idea is to counteract the disturbance $d(t)$ by means of two gains $k(t)$ and $\rho(t)$, which become an upper bound for the first and the second derivative of the disturbance. It is possible to demonstrate that the corresponding candidate Lyapunov function converges to 0, which means that the gains themselves are bounded, and converge to the unknown disturbance derivatives. An example of application of this technique (simulated with a step-size equal to 0.1 ms) is represented in Figs. 4(a)-4(d). There, the double-

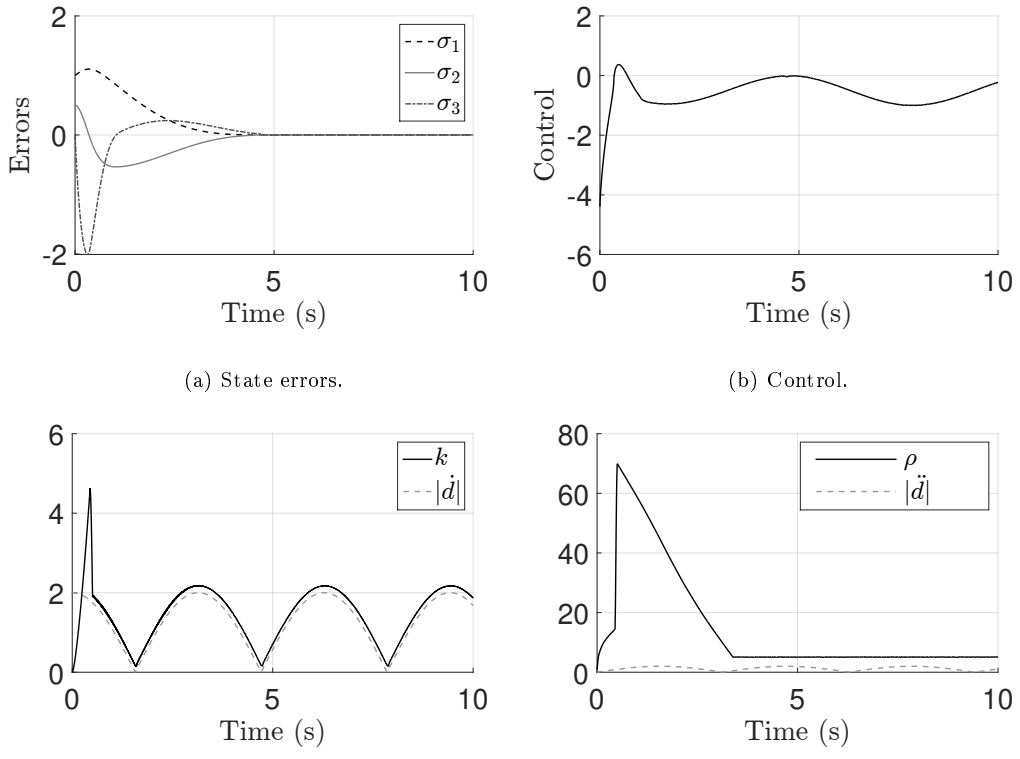

(a) State errors.

(b) Control.

(c) First adaptive gain.

(d) Second adaptive gain.

Fig. 4 Application of double-layer adaptive HOSM: step-size = 0.1 ms.

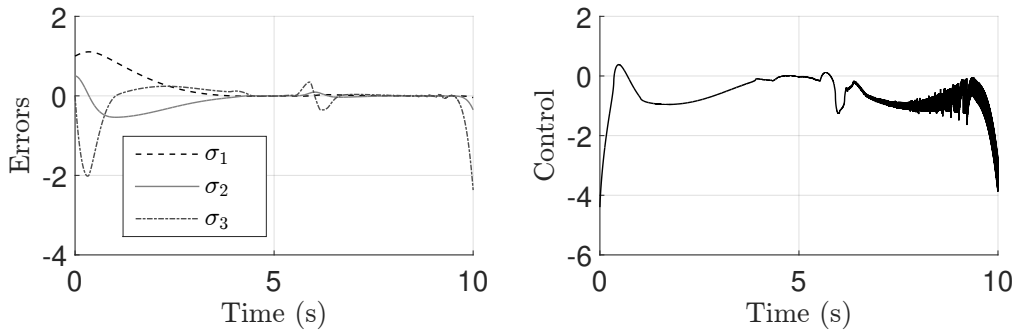

(a) State errors.

(b) Control.

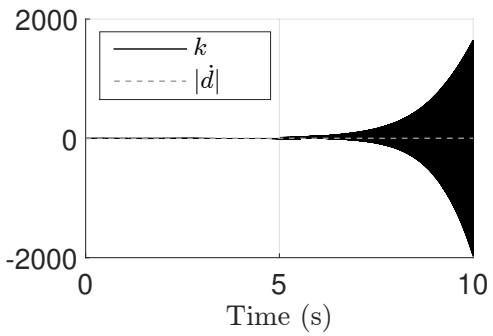

(c) First adaptive gain.

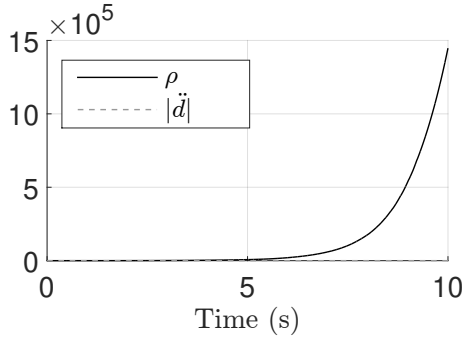

(d) Second adaptive gain.

Fig. 5 Application of double-layer adaptive HOSM: step-size = 2.5 ms.

layer based adaptive scheme is able to drive the states of the perturbed system, represented in Fig. 4(a) by using the control signal (depicted in Fig. 4(b)) to its equilibrium point. Figures. 4(c) and 4(d) show the two layers of gains k and ρ. They are integrated in the scheme to compensate for the disturbances. To guarantee convergence, the first gain has to be equal or greater than the absolute value of the first derivative of the disturbance. An example of this adaptive scheme is shown in Fig. 4(c), where the gain k tracks with some margin ϵ_k (which is one of the tuning parameters) $\left|\dot{d}(t)\right|$. The tracking of the disturbance is realized by using the second layer, defined by a further gain ρ, which is an upper bound for the second derivative of the disturbance $\ddot{d}(t)$, and ensures the convergence of the scheme. However, while there is formal proof for the theoretical stability of the scheme, in practice some numerical issues arise when larger step-sizes are taken. For instance if the step-size is increased to 2.5 ms, while keeping all the other parameters constant, we get the results depicted in Figs. 5(a)-5(d). One can see that numerical instabilities cause divergence of the states of the adaptive scheme, which directly causes the divergence of the states (Fig. 5(a)) . Therefore, while

this technique is an excellent choice for high-performance architectures, for machines with stricter CPU limitations, such as onboard computers, this algorithm may not be the best alternative.

To overcome this drawback an alternative scheme based on MIMO sliding-mode observer is proposed. The advantage is twofold: first, it significantly relaxes the step-size requirements, while still bringing the state errors to 0. Second, it provides the variables needed for the feedback process, that is σ, and its derivatives. Figures 6(a)-6(d) and 7(a)-7(d) show the corresponding results obtained by using the proposed ADHOSMC scheme for step-size equal to 0.1 and 2.5 ms, respectively. No qualitative differences can be observed in the states, which for both cases converge towards the equilibrium point of the system, and in the controls, which are chattering-free. Moreover, for both cases the disturbance observer converges in less than a second (about 690 ms) to the true $d(t)$ with an accuracy of $\pm 1\%$.

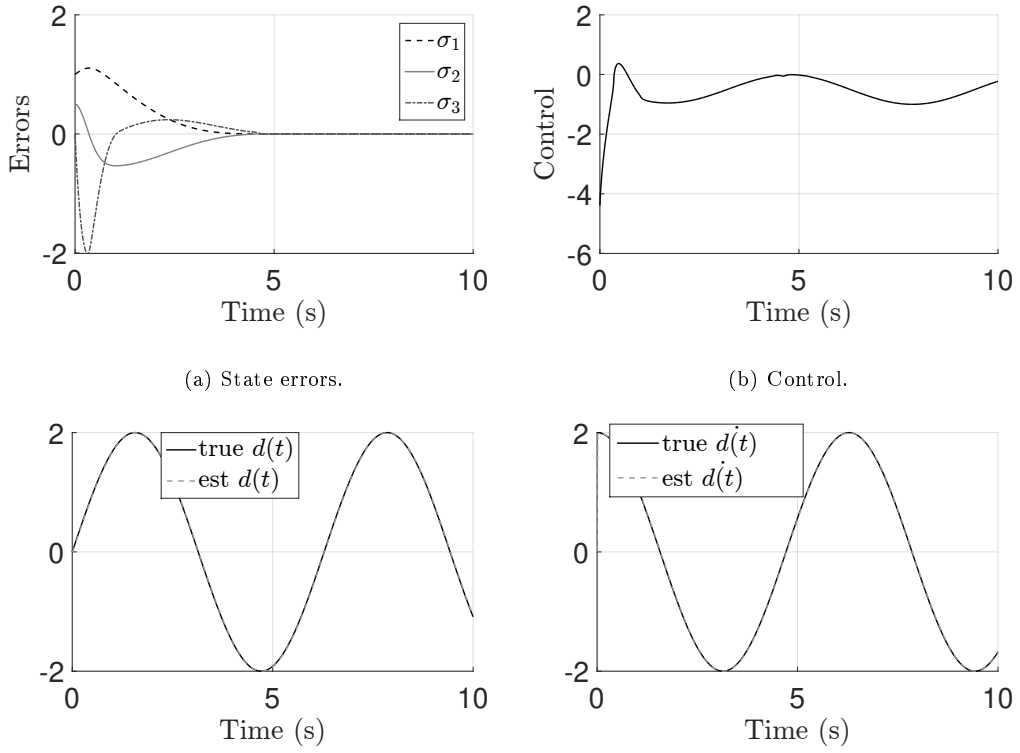

(a) State errors.

(b) Control.

(c) Disturbance estimation.

(d) Disturbance derivative estimation.

Fig. 6 Application of adaptive disturbance-based high-order SMC: step-size = 0.1 ms.

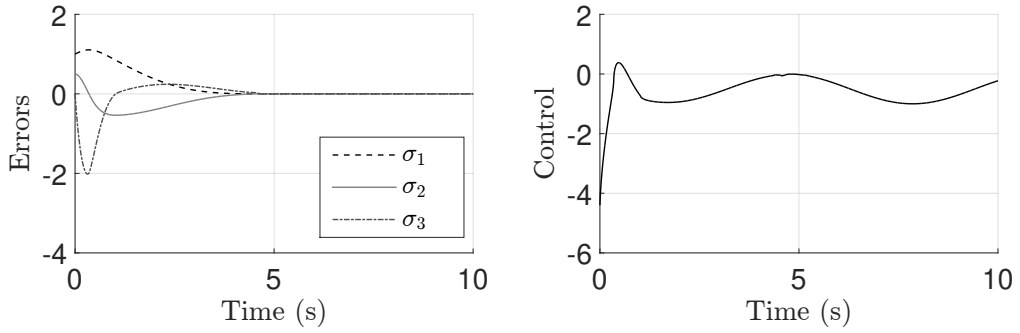

(a) State errors.

(b) Control.

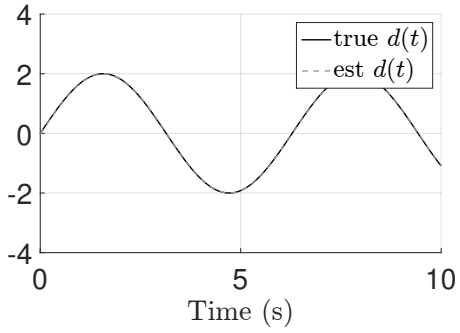

(c) Disturbance estimation.

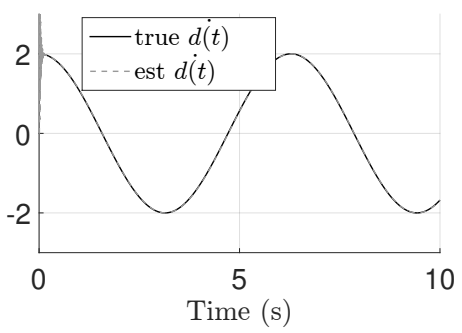

(d) Disturbance derivative estimation.

Fig. 7 Application of adaptive disturbance-based high-order SMC: step-size = 2.5 ms.

V. Longitudinal Controller Design

Let us now apply the approach discussed in the previous section to the longitudinal equations of motion of an unpowered re-entry vehicle. First, we need to extract the input/output linearized model from these equations, to have a system in the form of Eq. (2) to make the application of the ADHOSMC possible.

A. Input/Output Feedback Linearization

The longitudinal dynamics of the vehicle with respect to a non-rotating Earth is described by [10],

$$\begin{aligned}
\dot{h} &= V \sin\gamma \\
\dot{V} &= -D - g \sin\gamma \\
\dot{\gamma} &= \frac{1}{V} L \cos\mu + \left(\frac{V}{r} - \frac{g}{V} \right) \cos\gamma \\
\dot{\alpha} &= u_\alpha + \dot{\alpha}_{\text{ref}} \\
\dot{\mu} &= u_\mu + \dot{\mu}_{\text{ref}}
\end{aligned} \tag{17}$$

where h, V and γ are the altitude, the velocity modulus, and the flight-path angle, respectively, while r is the radial position. g is the gravity acceleration, while L and D are the lift and drag accelerations. The controls are in this case the angle-of-attack rate, u_α, and the bank-angle rate, u_μ. Indeed, they appear in affine form in the equations of motion. This is not the case for the angle of attack, which is "hidden" in the aerodynamic database (for the vehicle analyzed here the coefficients depend on angle of attack, Mach number and altitude), and the bank angle, which appears as an argument of the cosine function. The objective is to derive the MIMO ADHOSMC that allows to track the reference altitude $h_{\text{ref}}(t)$ and velocity $V_{\text{ref}}(t)$. An important difference with respect to [24], [25], and [39] is that in this case the reference states are time-dependent, and not terminal, constant values, therefore their derivatives are different from zero, and need to be included in the controller design. To have the controls linearly appearing in the equations of motion we differentiate the altitude three times, and the velocity two times. The total relative degree of the system is 5, and is equal to the order of the system of Eq. (17).

If we differentiate the altitude three times with respect to time, we get

$$\begin{aligned}
\dot{h}(t) &= V \sin\gamma \\
\ddot{h}(t) &= \dot{V} \sin\gamma + V \dot{\gamma} \cos\gamma \\
\dddot{h}(t) &= \ddot{V} \sin\gamma + 2\dot{V}\dot{\gamma} \cos\gamma + V\ddot{\gamma} \cos\gamma - V\dot{\gamma}^2 \sin\gamma
\end{aligned} \tag{18}$$

From the above equation it is clear that the expression for $\ddot{\gamma}$ is needed. If we differentiate γ twice,

we get

$$\begin{aligned}
\dot{\gamma} &= \frac{L}{V}\cos\mu + \left(\frac{V}{r} - \frac{g}{V}\right)\cos\gamma \\
\ddot{\gamma} &= \frac{\dot{L}}{V}\cos\mu - \frac{L\dot{V}}{V^2}\cos\mu - \frac{L\sin\mu}{V}(\dot{\mu}_{\text{ref}} + u_\mu) + ... \\
&+ \left(\frac{\dot{V}}{r} - \frac{V\dot{r}}{r^2} - \frac{\dot{g}}{V} + \frac{g\dot{V}}{V^2}\right)\cos\gamma - \left(\frac{V}{r} - \frac{g}{V}\right)\dot{\gamma}\sin\gamma
\end{aligned} \tag{19}$$

Furthermore, differentiating the velocity twice with respect to time yields

$$\begin{aligned}
\dot{V} &= -D - g\sin\gamma \\
\ddot{V} &= -\dot{D} - \dot{g}\sin\gamma - g\dot{\gamma}\cos\gamma
\end{aligned} \tag{20}$$

Atmospheric density and gravity acceleration derivatives with respect to time can be easily computed either analytically or numerically. Assuming that the atmospheric density ρ and the gravity acceleration g depend only on the altitude, we can write

$$\begin{aligned}
\dot{\rho} &= \rho_h \dot{h} \\
\dot{g} &= g_h \dot{h}
\end{aligned} \tag{21}$$

where ρ_h and g_h are the derivatives of the atmospheric density and the gravity acceleration with respect to the altitude, respectively. From the analysis of Eqs. (18)-(20) it is clear that we need to extract differential information about the aerodynamic accelerations L and D from the model. Drag and lift accelerations derivatives with respect to time can be computed as

$$\begin{aligned}
\dot{D} &= D\left(\frac{\dot{\rho}}{\rho} + 2\frac{\dot{V}}{V} + \frac{\dot{C}_D}{C_D}\right) \\
\dot{L} &= L\left(\frac{\dot{\rho}}{\rho} + 2\frac{\dot{V}}{V} + \frac{\dot{C}_L}{C_L}\right)
\end{aligned} \tag{22}$$

The time derivatives of the aerodynamic coefficients can be computed using the information contained in the aerodynamic database,

$$\begin{aligned}
\dot{C}_D &= C_{D,\alpha}\left(\dot{\alpha}_{\text{ref}} + u_\alpha\right) + C_{D,M}M_V\dot{V} + (C_{D,M}M_h + C_{D,h})\dot{h} \\
\dot{C}_L &= C_{L,\alpha}\left(\dot{\alpha}_{\text{ref}} + u_\alpha\right) + C_{L,M}M_V\dot{V} + (C_{L,M}M_h + C_{L,h})\dot{h}
\end{aligned} \tag{23}$$

where $C_{D,\alpha}$ and $C_{L,\alpha}$ are the derivative of the aerodynamic coefficients with respect to the angle of attack α. $C_{D,M}$ and $C_{L,M}$ are the derivative of the aerodynamic coefficients with respect to the Mach number M, $C_{D,h}$ and $C_{L,h}$ are the derivative of the aerodynamic coefficients with respect to the altitude, while $\dot{\alpha}_{\text{ref}}$ is the reference angle-of-attack rate. Finally, the terms M_V and M_h are the

derivatives of the Mach number with respect to the velocity V and the altitude h, and are described in the appendix. With all these relationships, the entire input/output model can be obtained. It has the following compact form

$$\begin{aligned} \dddot{h}(t) &= a_h + b_{h,\alpha} u_\alpha + b_{h,\mu} u_\mu \\ \ddot{V}(t) &= a_V + b_{V,\alpha} u_\alpha + b_{V,\mu} u_\mu \end{aligned} \tag{24}$$

As for the single-input, single-output (SISO) system of Eq. (5), uncertainties on aerodynamics, mass, atmosphere, and wind will cause variations of the functions a_i, $b_{i,j}$, $i = h, V$, $j = \alpha$, μ. All these uncertainties can be combined into two extra terms to be added in Eq. (24), which become

$$\begin{aligned} \dddot{h}(t) &= a_h + b_{h,\alpha} u_\alpha + b_{h,\mu} u_\mu + d_h \\ \ddot{V}(t) &= a_V + b_{V,\alpha} u_\alpha + b_{V,\mu} u_\mu + d_V \end{aligned} \tag{25}$$

The expressions for the terms a_h, a_V, $b_{h,\alpha}$, $b_{h,\mu}$, $b_{V,\alpha}$, $b_{V,\mu}$ are given in the appendix. They depend on the states and their derivatives, while u_α and u_μ are the control rates we need to determine.

Remark 5. Explicit expressions for the uncertainties d_h and d_V can be obtained by writing the perturbed version of Eqs. (25), which can be obtained by replacing the nominal variables involved in Eqs. (18)-(24) with their perturbed version (i.e. replacing C_L with $C_L + \Delta C_L$, and so on). However, this development is omitted, as the scope of the adaptive control scheme proposed here is to reconstruct uncertainties without any previous knowledge of them. Moreover, there may be other uncertainties not modeled by Eqs. (18)-(24), which will be dealt with the method here anyway.

It is now possible to design the adaptive high-order sliding-mode control scheme for the system of Eq. (25).

B. MIMO adaptive disturbance-based high-order sliding mode control

The objective of the feedback control scheme is to track the given altitude and velocity profiles. In a similar fashion to what has been done in Sec. III, let us define two decoupled sliding surfaces σ_h and σ_V,

$$\begin{aligned} \sigma_h &= h(t) - h_{\text{ref}}(t) \\ \sigma_V &= V(t) - V_{\text{ref}}(t) \end{aligned} \tag{26}$$

We can extend the approach developed in Sec. III, and specifically Eq. (14) to the MIMO system represented by Eq. (26). Let us define the following matrices and vectors:

$$\mathbf{A} = \begin{bmatrix} a_h \\ \\ a_V \end{bmatrix}, \ \mathbf{B} = \begin{bmatrix} b_{h,\alpha} & b_{h,\mu} \\ \\ b_{V,\alpha} & b_{V,\mu} \end{bmatrix}, \ \mathbf{D} = \begin{bmatrix} d_h \\ \\ d_V \end{bmatrix} \tag{27}$$

$$\tilde{\mathbf{u}} = \begin{bmatrix} \sum_{i=0}^{2} \gamma_{h,i} \left| \sigma_h^{(i)}(t) \right|^{\alpha_{h,i}} \operatorname{sgn}\left(\sigma_h^{(i)}(t)\right) \\ \sum_{i=0}^{1} \gamma_{V,i} \left| \sigma_V^{(i)}(t) \right|^{\alpha_{V,i}} \operatorname{sgn}\left(\sigma_V^{(i)}(t)\right) \end{bmatrix}, \ \mathbf{u} = \begin{bmatrix} u_\alpha \\ \\ u_\mu \end{bmatrix} \tag{28}$$

With these definitions, the MIMO control law can be written in matrix form as

$$\mathbf{u} = -\mathbf{B}^{-1}\left(\tilde{\mathbf{u}} + \mathbf{A} + \mathbf{D}\right) \tag{29}$$

All the terms in Eq. (29) are defined, except the vector $\mathbf{D}$, which will be replaced by its estimated value $\widehat{\mathbf{D}}$, leading to the final form of the ADHOSMC law.

$$\mathbf{u} = -\widehat{\mathbf{B}}^{-1}\left(\tilde{\mathbf{u}} + \widehat{\mathbf{A}} + \widehat{\mathbf{D}}\right) \tag{30}$$

The quantities $\widehat{\mathbf{A}}$, $\widehat{\mathbf{B}}$ are computed by using the nominal expressions described in the appendix, by using the derivatives estimated with the SMO, and $\widehat{\mathbf{D}}$ is the vector containing the online estimates of the disturbances acting on the system. From the terms $\mathbf{u}$, the angle of attack and bank angle can be obtained as

$$\begin{aligned} \alpha(t) &= \alpha_{\text{ref}}(t) + \Delta\alpha(t) = \alpha_{\text{ref}}(t) + \int_{t_0}^{t} u_\alpha d\tau \\ \mu(t) &= \mu_{\text{ref}}(t) + \Delta\mu(t) = \mu_{\text{ref}}(t) + \int_{t_0}^{t} u_\mu d\tau \end{aligned} \tag{31}$$

where u_α and u_μ are the feedback angle-of-attack rate and the bank-angle rate, respectively. From the inspection of Eq. (30) one can see that the control can be synthesized only if the matrix $\mathbf{B}$ is non-singular.

$$\det(\mathbf{B}) = b_{h,\alpha} b_{V,\mu} - b_{h,\mu} b_{V,\alpha} \neq 0 \tag{32}$$

If we look at the definitions shown in the appendix, we can write

$$\det(\mathbf{B}) = 0 \Leftrightarrow b_{D,\alpha} L \cos\gamma \sin\mu = 0 \tag{33}$$

Since $b_{D,\alpha}$ and L are always different from 0, from a physical point of view Eq. (33) gives us the two only possibilities where the control synthesis cannot be applied. The former is related to the condition $\gamma = \pm 90$ deg, which means that the controller cannot be applied in vertical motion. This condition is excluded during the trajectory planning in any case. The latter is related to the condition $\mu = 0$ deg, which represents a well-known singularity for controllability of unpowered entry vehicles [40–42]. To exclude this possibility, a region around $\mu = 0$ deg is avoided. Specifically, for all the simulations the bank angle is limited in the interval $[0.1, 89]$ deg. The angle-of-attack was limited to the range $[-5, 7.5]$ deg with respect to the nominal angle-of-attack profile, in a similar fashion to what has been done for the Space Shuttle [10]. With the proposed approach it is possible to track the altitude and the velocity by modulating the bank angle and the angle of attack at the same time. The next step is the extension of the sliding-mode observer to the system represented by Eq. (25).

C. Nonlinear Disturbance Observer

The control scheme synthesized in the previous section relies on several models (for instance, the atmospheric density and the aerodynamic database), which can be different with respect to the actual data. The missing information can be enclosed in $\widehat{\mathbf{D}}$, which will be estimated by a MIMO SMO. The technique is here extended to the longitudinal states involved in the atmospheric entry, that is, the altitude and the velocity. Moreover, since the flight-path angle and its derivatives appear in Eqs. (18)-(24), this state is also included in the observer, which will provide, together with the states and their derivatives, the estimates $\widehat{d_h}(t)$ and $\widehat{d_V}(t)$. If we define the state vector $\mathbf{x}$ as

$$\mathbf{x} = \left\{ \begin{array}{ccccccc} h & \dot{h} & \ddot{h} & v & \dot{v} & \gamma & \dot{\gamma} \end{array} \right\}^T \tag{34}$$

the system of Eq. (17) can be rewritten in state-space form as

$$\begin{aligned}
\dot{x}_1 &= x_2 \\
\dot{x}_2 &= x_3 \\
\dot{x}_3 &= a_h + b_{h,\alpha} u_\alpha + b_{h,\mu} u_\mu \\
\dot{x}_4 &= x_5 \\
\dot{x}_5 &= a_V + b_{V,\alpha} u_\alpha + b_{V,\mu} u_\mu \\
\dot{x}_6 &= x_7 \\
\dot{x}_7 &= a_\gamma + b_{\gamma,\alpha} u_\alpha + b_{\gamma,\mu} u_\mu
\end{aligned} \tag{35}$$

We want to estimate online the terms $\widehat{d}_h(t)$ and $\widehat{d}_V(t)$ defined in Eq. (25). If we define the new augmented state vector $\mathbf{x}_a$

$$\mathbf{x}_a = \left\{ \begin{array}{cccccccccc} h & \dot{h} & \ddot{h} & d_h & v & \dot{v} & d_V & \gamma & \dot{\gamma} \end{array} \right\}^T \tag{36}$$

the perturbed equations of motion can be represented in state-space form as

$$\begin{aligned}
\dot{x}_{a,1} &= x_{a,2} \\
\dot{x}_{a,2} &= x_{a,3} \\
\dot{x}_{a,3} &= a_h + b_{h,\alpha} u_\alpha + b_{h,\mu} u_\mu + x_{a,4} \\
\dot{x}_{a,4} &= \dot{d}_h \\
\dot{x}_{a,5} &= x_{a,6} \\
\dot{x}_{a,6} &= a_V + b_{V,\alpha} u_\alpha + b_{V,\mu} u_\mu + x_{a,7} \\
\dot{x}_{a,7} &= \dot{d}_V \\
\dot{x}_{a,8} &= x_{a,9} \\
\dot{x}_{a,9} &= a_\gamma + b_{\gamma,\alpha} u_\alpha + b_{\gamma,\mu} u_\mu
\end{aligned} \tag{37}$$

For the scenario analyzed here the measurements of attitude, position and velocity are obtained with sufficient accuracy by the navigation subsystem [38], and are converted into altitude, velocity and flight-path angle measurements z_h, z_V, and z_γ. These measurements can be integrated into the

following MIMO nonlinear disturbance estimator,

$$\begin{aligned}
\dot{\widehat{x}}_{a,1} &= \widehat{x}_{a,2} + \lambda_0^h \tilde{x}_h + \kappa_0^h \,\mathrm{sat}\,(\tilde{x}_h) \\
\dot{\widehat{x}}_{a,2} &= \widehat{x}_{a,3} + \lambda_1^h \tilde{x}_h + \kappa_1^h \,\mathrm{sat}\,(\tilde{x}_h) \\
\dot{\widehat{x}}_{a,3} &= a_h + b_{h,\alpha} u_\alpha + b_{h,\mu} u_\mu + \widehat{x}_{a,4} + \lambda_2^h \tilde{x}_h + \kappa_2^h \,\mathrm{sat}\,(\tilde{x}_h) \\
\dot{\widehat{x}}_{a,4} &= \lambda_3^h \tilde{x}_h + \kappa_3^h \,\mathrm{sat}\,(\tilde{x}_h) \\
\dot{\widehat{x}}_{a,5} &= \widehat{x}_{a,6} + \lambda_0^v \tilde{x}_h + \kappa_0^v \,\mathrm{sat}\,(\tilde{x}_V) \\
\dot{\widehat{x}}_{a,6} &= a_V + b_{V,\alpha} u_\alpha + \widehat{x}_{a,7} + \lambda_1^v \tilde{x}_V + \kappa_1^v \,\mathrm{sat}\,(\tilde{x}_V) \\
\dot{\widehat{x}}_{a,7} &= \lambda_2^v \tilde{x}_V + \kappa_2^v \,\mathrm{sat}\,(\tilde{x}_V) \\
\dot{\widehat{x}}_{a,8} &= \widehat{x}_{a,9} + \lambda_0^\gamma \tilde{x}_\gamma + \kappa_0^\gamma \,\mathrm{sat}\,(\tilde{x}_\gamma) \\
\dot{\widehat{x}}_{a,9} &= a_\gamma + b_{\gamma,\alpha} u_\alpha + b_{\gamma,\mu} u_\mu + \lambda_1^\gamma \tilde{x}_\gamma + \kappa_1^\gamma \,\mathrm{sat}\,(\tilde{x}_\gamma)
\end{aligned} \tag{38}$$

where λ_i^h, λ_i^v, λ_i^γ are the linear gains, and κ_i^h, κ_i^v, κ_i^γ are the nonlinear gains of the observer respectively; they are all positive, while the terms $\tilde{x}_h$, $\tilde{x}_V$, $\tilde{x}_\gamma$ are the differences between the measurements and the observer estimates, computed as

$$\begin{aligned}
\tilde{x}_h &= z_h - \hat{x}_{a,1} \\
\tilde{x}_V &= z_V - \hat{x}_{a,5} \\
\tilde{x}_\gamma &= z_\gamma - \hat{x}_{a,8}
\end{aligned} \tag{39}$$

The state vector $\widehat{\mathbf{x}}_a$ is consequently defined as

$$\widehat{\mathbf{x}}_a = \left\{ \begin{array}{ccccccccc} \widehat{h} & \dot{\widehat{h}} & \ddot{\widehat{h}} & \widehat{d}_h & \widehat{v} & \dot{\widehat{v}} & \widehat{d}_V & \widehat{\gamma} & \dot{\widehat{\gamma}} \end{array} \right\}^T \tag{40}$$

To avoid observer's chattering, the sgn function is replaced by the saturation function, defined as

$$\mathrm{sat}\,(\tilde{x}_m) = \begin{cases} 1, & \tilde{x}_m \geq w_m \\ -1, & x \leq -w_m \\ \frac{\tilde{x}_m}{w_m}, & |\tilde{x}_m| < w_m \end{cases}, \quad m = h, v, \gamma \tag{41}$$

Equation (41) implies that when the residuals defined in Eq. (39) are within the boundaries defined by w_h, w_V, and w_γ, the SMO becomes a Luenberger observer with augmented linear gains

$$\tilde{\lambda}_i^m = \lambda_i^m + \tfrac{1}{w_m} \quad m = h, v, \gamma \tag{42}$$

The procedure to select the linear and nonlinear gains is directly taken from [37], and is based on the assumption that the disturbances and their derivatives can be unknown, but bounded, which

is a realistic hypothesis given the scenario we are dealing with. Therefore, it is always possible to define some positive constants c_i^m, $m = h, v$, and $i = 1, 2$ such that

$$\begin{aligned} |d_h| \leq c_1^h, \;\; |\dot{d}_h| \leq c_2^h \\ |d_V| \leq c_1^v, \;\; |\dot{d}_V| \leq c_2^v \end{aligned} \tag{43}$$

holds. More rigorously, the disturbance derivatives are assumed Lipschitz continuous. With these premises, it is possible to realize the conditions for the SMO only if the nonlinear gains satisfy the following relationships [36]:

$$\begin{aligned} \kappa_1^h \geq & |\tilde{x}_{a,2}| \\ \kappa_1^V \geq & |\tilde{x}_{a,5}| \\ \kappa_1^\gamma \geq & |\tilde{x}_{a,8}| \end{aligned} \tag{44}$$

If we define the thresholds for the convergence of the observer ϵ_h, ϵ_V, and ϵ_γ it is possible to compute the linear gains as

$$\begin{aligned} \lambda_i^h &= C_4^i \mu_h^i, \;\; i = 1, \ldots, 4 \\ \lambda_i^V &= C_3^i \mu_V^i, \;\; i = 1, \ldots, 3 \\ \lambda_i^\gamma &= C_1^i \mu_\gamma^i, \qquad i = 1, 2 \end{aligned} \tag{45}$$

where the parameters μ_h, μ_V, and μ_γ are the poles of the Luenberger observer. These parameters have to satisfy the following inequality,

$$\mu_m \geq \sqrt{\frac{\mu_{max}(\mathbf{P}_m)}{\mu_{min}(\mathbf{P}_m)}} \frac{2\mu_{max}(\mathbf{P}_m) c_2^m}{(1-\nu_m)\epsilon_m}, \;\; m = h, v, \gamma \tag{46}$$

where the terms ν_h, ν_V, and ν_γ are constant parameters defined in the range (0,1). The coefficients C_j^i are computed as

$$C_j^i = \frac{j!}{i!(j-i)!} \;\; i, j = 1, 2, 3 \tag{47}$$

and the parameters $\mu_{max}(\mathbf{P}_m)$ and $\mu_{min}(\mathbf{P}_m)$ $(m = h, v, \gamma)$, are the maximum and the minimum eigenvalues of the matrices P_m, which represent the solutions of the following Lyapunov equations

$$\begin{aligned} \mathbf{P}_h \mathbf{M}_h + \mathbf{M}_h^T \mathbf{P}_h &= -\mathbf{I}_3 \\ \mathbf{P}_V \mathbf{M}_V + \mathbf{M}_V^T \mathbf{P}_V &= -\mathbf{I}_2 \\ P_\gamma M_\gamma + M_\gamma^T P_\gamma &= -1 \end{aligned} \tag{48}$$

with

$$\mathbf{M}_h = \begin{bmatrix} -C_3^1 & 1 & 0 \\ -C_3^2 & 0 & 1 \\ -C_3^3 & 0 & 0 \end{bmatrix}, \ \mathbf{M}_V = \begin{bmatrix} -C_2^1 & 1 \\ -C_2^2 & 0 \end{bmatrix}, \ M_\gamma = -C_1^1 \tag{49}$$

and $\mathbf{I}_n$ is the identity matrix having dimensions $n \times n$. Once the linear gains are computed, the nonlinear gains can be obtained as

$$\kappa_1^m \geq \|\tilde{x}_m\|_{max} \sqrt{\frac{\mu_{max}(\mathbf{P}_m)}{\mu_{min}(\mathbf{P}_m)}}, \ m = h, v, \gamma \tag{50}$$

$$\begin{aligned} \kappa_i^h &\geq \kappa_1^h C_3^{i-1} \mu_h^{i-1}, \ i = 2, 3, 4 \\ \kappa_i^v &\geq \kappa_1^v C_2^{i-1} \mu_V^{i-1}, \quad i = 2, 3 \\ \kappa_i^\gamma &\geq \kappa_1^\gamma C_1^{i-1} \mu_\gamma^{i-1}, \quad i = 2 \end{aligned} \tag{51}$$

Rigorous mathematical proofs for these relationships can be found in [37].

With the estimates of the disturbances $\widehat{d}_h(t)$ and $\widehat{d}_V(t)$, and the states' derivatives $\dot{\widehat{h}}(t)$, $\ddot{\widehat{h}}(t)$, $\dddot{\widehat{h}}(t)$, $\dot{\widehat{V}}(t)$, $\ddot{\widehat{V}}(t)$, the sliding variables can finally be computed as

$$\begin{aligned} \widehat{\sigma}_h &= h(t) - h_{\text{ref}}(t) \\ \dot{\widehat{\sigma}}_h &= \dot{\widehat{h}}(t) - \dot{h}_{\text{ref}}(t) \\ \ddot{\widehat{\sigma}}_h &= \ddot{\widehat{h}}(t) - \ddot{h}_{\text{ref}}(t) \\ \widehat{\sigma}_V &= \widehat{V}(t) - V_{\text{ref}}(t) \\ \dot{\widehat{\sigma}}_V &= \dot{\widehat{V}}(t) - \dot{V}_{\text{ref}}(t) \end{aligned} \tag{52}$$

With the use of the disturbance observer, we simultaneously estimate online the uncertainties acting on the system, and the derivatives of the current states, needed for the design of the controller, by only using available measurements.

VI. Results

Simulation campaigns have been performed to assess the behavior of the proposed controller. The ADHOSMC is compared with a standard SMC, based on the traditional sliding-mode control theory [39]. The schemes are tuned to ensure similar control authority. More specifically, the

two seeds α_h and α_V are both taken equal to 0.8, while the poles associated with Eq. (28) are placed at -0.4 and -0.6, respectively. For what regards the disturbance observer, the linear gains are based on the poles $\lambda_h = -6.18$, $\lambda_V = -4.57$, and $\lambda_\gamma = -5.56$, while the the nonlinear gains are $\kappa^h = [2.82,\ 78.4,\ 484.9,\ 1664.7]^T$, $\kappa^V = [0.51,\ 5.1,\ 11.7]$, and $\kappa^\gamma = [0.02,\ 0.17]$. Finally, the saturation layers are chosen as $w_h = 0.25$, $w_V = 0.1$, and $w_\gamma = 0.001$. The nonlinear control strategy is therefore completely defined by a small number of constant parameters, with the advantage that no large data-sets, coming from gain-scheduling techniques, are required. For what regards the triggering of the feedback scheme, since at the beginning of the entry the atmospheric density is thin, the aerodynamic accelerations are very small and cannot properly counteract gravity, and this condition may induce control saturation. To avoid it, the scheme is triggered once the aerodynamic accelerations become significant. A rule, which works well in practice, is to use the drag-to-gravity ratio as measure of the effectiveness of the control. In this case the trigger is associated with a drag acceleration equal to $0.5g$, which happens in a time interval between 140 and 170 s after the beginning of the entry.

To assess the behavior of the developed control strategy, a full Monte-Carlo campaign has been run. Dispersions on atmospheric density, altitude, velocity and flight-path angle are considered. Moreover, aerodynamic dispersions, and mass uncertainty have been included. The control sample rate for all the simulations is 0.1 s. All the uncertainties follow a normal distribution. Further details about the uncertainties are listed in Table 2.

Table 2 Monte-Carlo campaign parameters.

Parameter	Range (3σ)	Units
Δh	± 1	km
ΔV	± 100	m/s
$\Delta\gamma$	± 0.25	deg
$\Delta\rho$	$\pm 20\%$	-
ΔC_L	$\pm 10\%$	-
ΔC_D	$\pm 10\%$	-
Δm	$\pm 0.5\%$	-

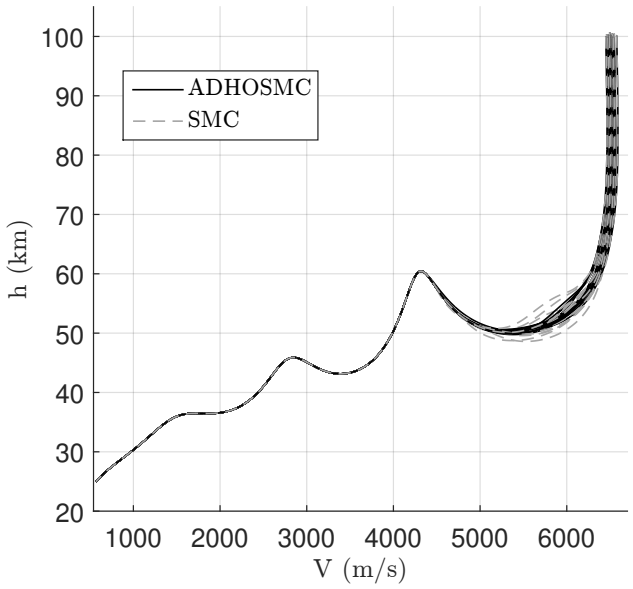

Fig. 8 MC campaign (1000 runs): ADHOSMC vs SMC - altitude velocity plane.

From the previous table one can see that, together with the initial errors and the atmospheric-density uncertainty, a variation of the C_L and C_D coefficients up to $\pm 10\%$ is included. These limits are in line with the wind-tunnel tests performed by the DLR Institute of Aerodynamics and Flow Technology [43]. Moreover, uncertainties in the dry mass, together with the propellant residuals were taken into account according to the margins suggested by the European Space Agency (ESA)[44]. A total of 1000 runs has been performed. For visibility purposes, only the results associated with the first 25 simulations are plotted, and are shown in Figs. 8 - 14, while in Figs. 15(a) and 15(b) there is a comparison of the behavior of the sliding states for all the three SMC techniques considered here. Table 3 illustrates the benefits of using ADHOSMC compared to SMC and pure HOSM.

From Fig. 8 and 9 we can observe that both the ADHOSMC and the SMC strategies correctly track the reference states. The dispersions reduce over time, and a first difference in the methods can be seen. The ADHOSMC generates smoother results, and this is especially visible in the $h-V$ plane, plotted in Fig. 8, and in the flight-path angle (Fig. 9(c)), in the interval between 140 and 170 s, which is exactly the moment at which the drag becomes large enough to counteract gravity. Note that the effective error that the control scheme has to deal with is much larger than what has been summarized in Table 2. Indeed, there is a lack of control authority during the first 2-3 minutes

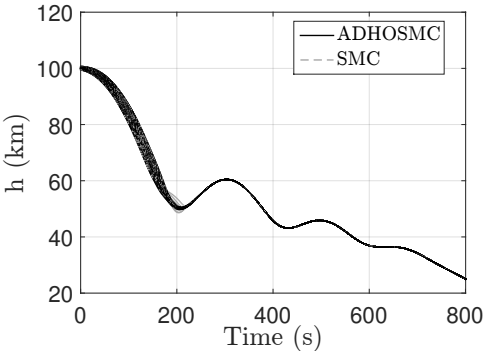

(a) ADHOSMC vs SMC: altitude.

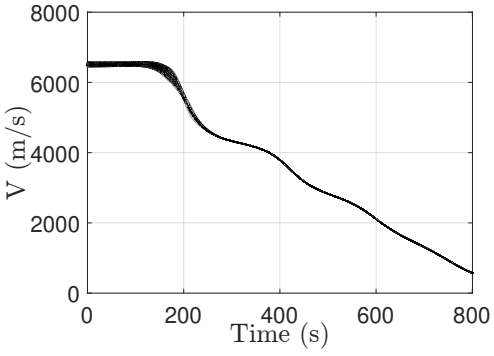

(b) ADHOSMC vs SMC: velocity.

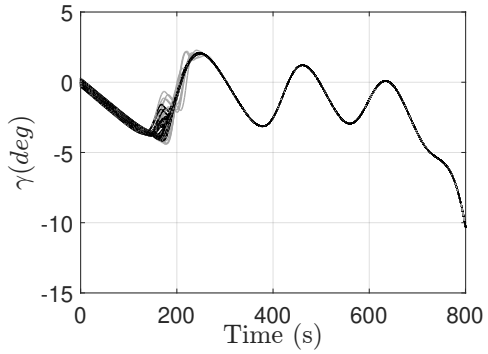

(c) ADHOSMC vs SMC: flight-path angle.

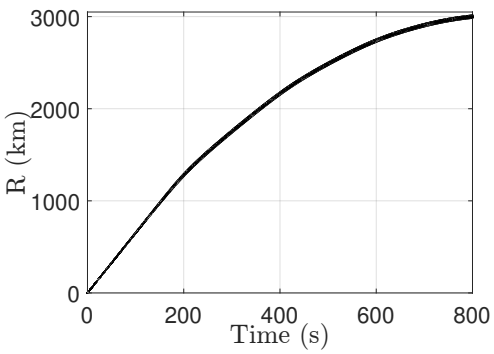

(d) ADHOSMC vs SMC: range.

Fig. 9 MC campaign (1000 runs): ADHOSMC vs SMC - states.

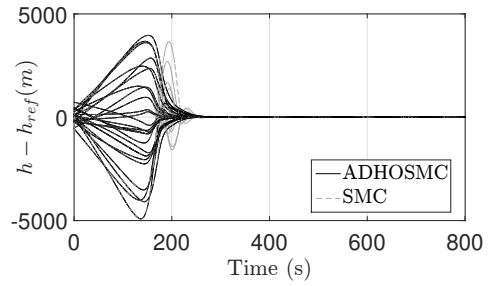

(a) ADHOSMC vs SMC: altitude error.

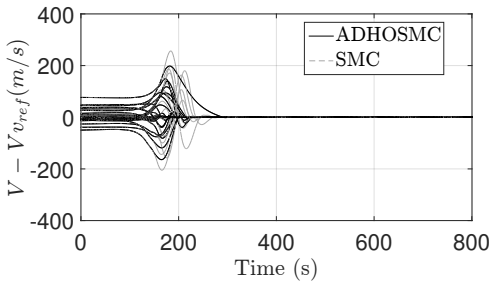

(b) ADHOSMC vs SMC: velocity error.

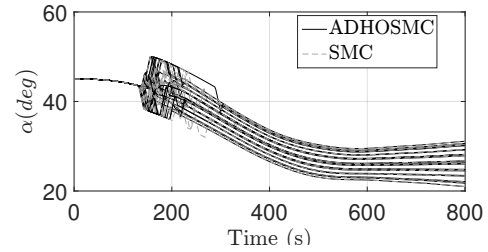

(c) ADHOSMC vs SMC: angle of attack.

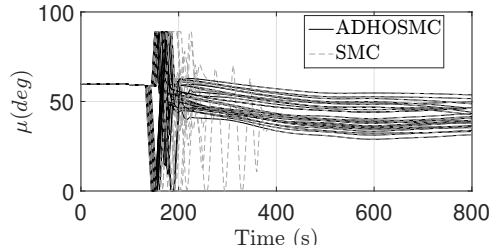

(d) ADHOSMC vs SMC: bank angle.

Fig. 10 MC campaign (1000 runs): ADHOSMC vs SMC - state errors and controls.

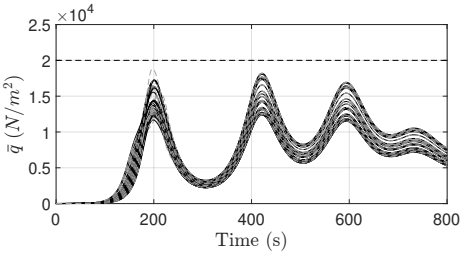

(a) ADHOSMC vs SMC: dynamic pressure.

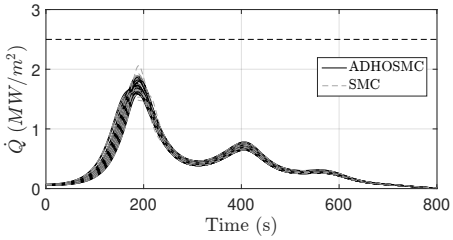

(b) ADHOSMC vs SMC: heat flux.

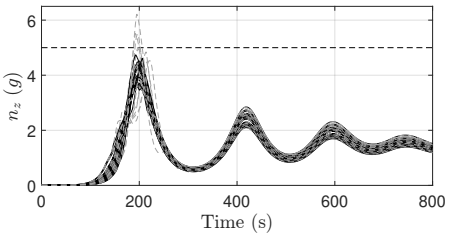

(c) ADHOSMC vs SMC: load factor.

Fig. 11 MC campaign (1000 runs): ADHOSMC vs SMC - constraints.

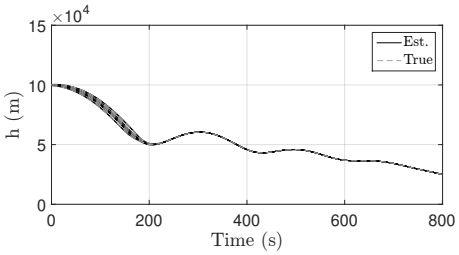

(a) Altitude.

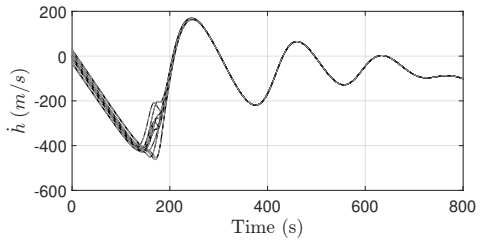

(b) Altitude 1st derivative.

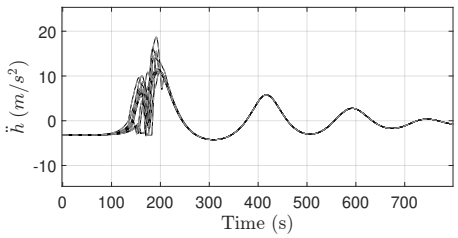

(c) Altitude 2nd derivative.

Fig. 12 MC campaign (1000 runs): altitude online reconstruction.

of mission, and during this phase the error may significantly increase. However the control scheme can properly counteract the error once activated. The difference coming from the two strategies become more evident in Figs. 10(a) and 10(b), where one can see that in general the convergence to the equilibrium point is significantly faster (in the order of 80-100 s) than if we use the standard

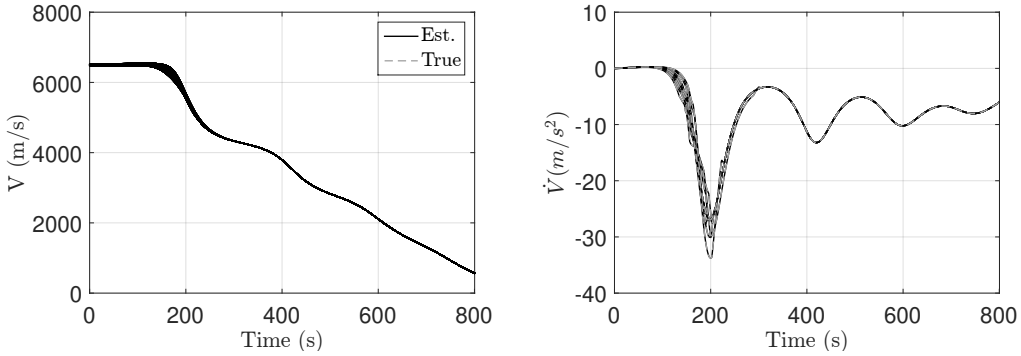

(a) Velocity.

(b) Velocity 1st derivative.

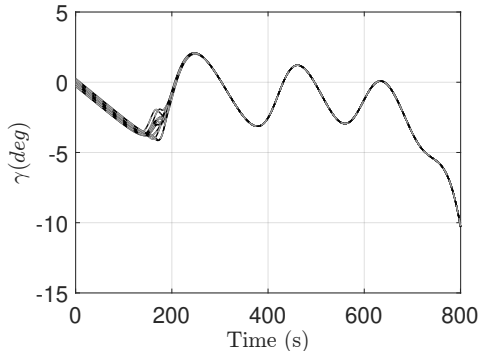

(c) Flight-path angle.

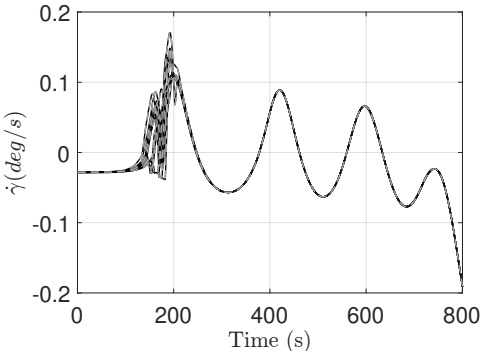

(d) Flight-path angle 1st derivative.

Fig. 13 MC campaign (1000 runs): velocity and flight-path angle reconstruction.

SMC. For the 1000 cases analyzed the velocity errors goes to 0 more slowly by using the ADHOSMC strategy than by using SMC in less than 1% of the cases, while for the altitude it never happens. The reason is due to an angle-of-attack saturation. In that case, the other available control, that is, the bank angle, is used to keep tracking the reference altitude, and this causes a delay in the convergence of the velocity error.

Note that in general, however, there is more control activity when the SMC is used than when the ADHOSMC is adopted, as is shown in Fig. 10. It is also interesting to see that once the sliding surfaces are reached, the control profiles of the two schemes perfectly overlap.

This behavior is consistent with the fact that the two control scheme achieve the same sliding surfaces in different ways, and in different times, but when these are reached, the control activity to track them is the same, as the kinematic profiles involved in their definition are the same too.

An interesting difference between the two schemes can be observed in Fig. 11, which shows

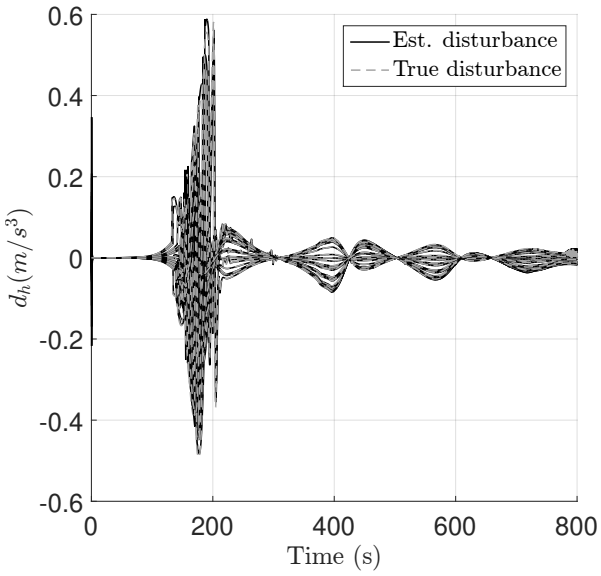

(a) Altitude disturbance.

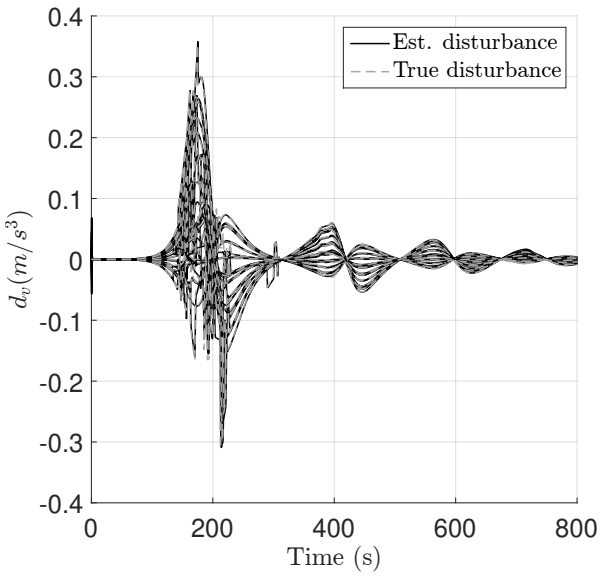

(b) Velocity disturbance.

Fig. 14 MC campaign (1000 runs): disturbances reconstruction.

the constraints. While both the control systems satisfy the limits in terms of dynamic pressure and heat flux, the delay in the convergence of the SMC with respect to the ADHOSMC causes several violations of the maximum value of vertical load factor, as it is visible from the bottom plot. This limit was violated in about 11% of the cases, while in total only six violations occur when the ADHOSMC is employed. The maximum violation in the two cases is in any case quite different.

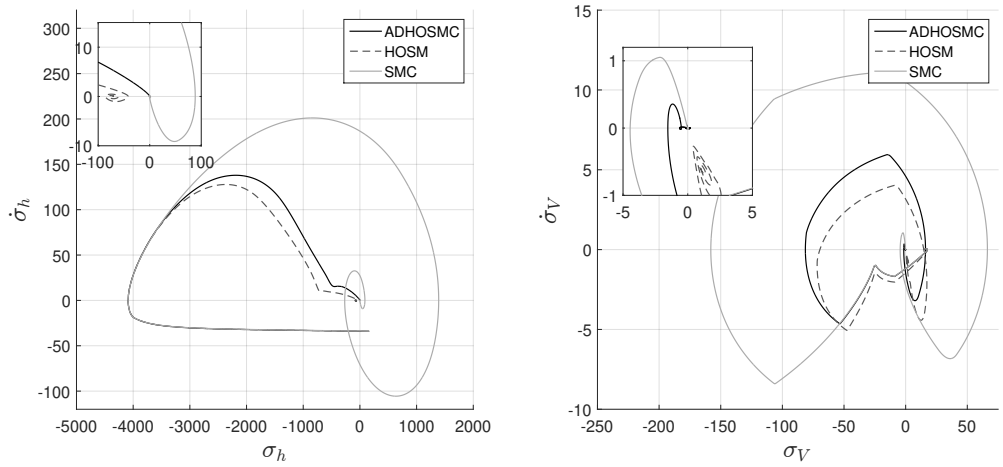

(a) Altitude sliding variables.

(b) Velocity sliding variables.

Fig. 15 MC campaign (1000 runs): ADHOSMC vs SMC - state errors.

The worst cases in terms of load factor are associated with a value of 5.27g (ADHOSMC) and 7.06g (SMC). Moreoer the conventional SMC violates 5 times the maximum dynamic pressure, while this never happens with the ADHOSMC. Finally, both the systems satisfy the requirements in terms of heat-flux.

In terms of observer's performance we can see how the states and their derivatives are correctly reconstructed. Specifically, the altitude and its first and second derivatives are shown in Fig. 12, while in Fig. 13 the velocity modulus, the flight-path angle, and their derivatives are plotted. The online estimates (continuous black lines) are overlapped with the corresponding true profiles (dotted gray lines). The estimates are very accurate over the entire mission timeline. Figures 14(a) and 14(b) show the comparison between true disturbances acting on the system ($d_h(t)$ and $d_V(t)$, in dotted, gray lines), and their estimates, ($\widehat{d}_h(t)$ and $\widehat{d}_V(t)$, in continuous, black lines). Also here the approximation is very good with one exception. Errors with respect to the true disturbances can indeed be observed only at the moment of triggering the feedback control scheme. The reason for this behavior resides in the fact that there is a discontinuity in the angular rates u_α and u_μ at the moment of triggering the control system or saturating the controls. Since they appear in the online sliding-mode observer of Eq. (38), the condition of Lipschitz continuity invoked in Eq. (43) is locally violated, and this causes the presence of these errors. However, once the control activity is started,

the hypothesis of Lipschitz continuity is valid again, and the estimated disturbances converge to the true ones immediately, and are bounded by the theoretical ϵ (assumed equal to 0.01 m/s^3 for both the altitude and the velocity), as foreseen by the SMO theory. In any case, since the local discontinuity of the angular rates is a mathematical simplification, it does not limit the practical applicability for real systems, which will always have a finite angular acceleration, and therefore will not be affected by this local decrease of accuracy. Finally, the behavior of the altitude and velocity sliding states for the three SMC techniques are depicted in Figs. 15(a) and 15(b). In both the plots one can see that the use of the disturbance observer help the ADHOSMC to reach the sliding surfaces, while without the control system does not reach the origin of the sliding state space. Note that the conventional SMC is also able to reach the origin, but it shows a worse transient, consistently with the results of Figs. 10(a) and 10(b).

Table 3 MonteCarlo campaign results.

Parameter	Units	ADHOSMC	SMC	HOSM
mean Δh_f	m	2.44	3.66	-27.92
std Δh_f	m	19.69	28.25	68.12
mean ΔV_f	m/s	-0.04	-0.01	-0.81
std ΔV_f	m/s	0.18	0.05	1.07
mean ΔR_f	km	0.50	0.99	0.90
std ΔR_f	km	7.43	7.71	7.82
mean $\bar{q}_{peak}$	N/m^2	15,226	15,391	15,295
std $\bar{q}_{peak}$	N/m^2	1,695	1,831	1,556
mean $\dot{Q}_{peak}$	MW/m^2	1.744	1.753	1.748
std $\dot{Q}_{peak}$	MW/m^2	0.089	0.124	0.079
mean $n_{z,peak}$	g	4.091	4.309	4.100
stand. dev. $n_{z,peak}$	g	0.284	0.610	0.277

If we look at Table 3 we can see the benefits of using the ADHOSMC: the tracking error in terms of altitude is reduced, both with respect to the standard SMC, and more dramatically with respect to the application of the corresponding pure HOSM strategy. Also the standard deviation is reduced of about 30% with respect to what is obtained by using the standard SMC. It is worth to

recall that these results are obtained without any saturation function in the control law (as in the case of the SMC), which would cause a decrease of the robustness of the system, and no trade-off between robustness and chattering reduction need to be operated.

Also in terms of final range, we can observe an improvement coming from the use of the proposed approach. The use of the ADHOSMC positively affects all the constraints. We can observe that all the peaks are equal or less to the ones obtained by using conventional SMC, and as previously stated, only six violations was observed on a total of 1000 cases (corresponding to the 0.6% of cases, against 112 violations observed when the SMC was used. Finally, the corresponding standard deviations are positively influenced as well when the ADHOSMC is employed. The reason for these results comes from the improvement in the transient behavior. Since all the peaks are experienced at about 180-200 s after the beginning of the entry, a better transient (i.e., a faster and smoother convergence to the reference states) automatically turns into a reduction of the peaks, which will become closer to the nominal ones.

VII. Conclusions

In this paper we have proposed a novel adaptive control scheme for hypersonic entry vehicles. The proposed method uses the chattering-free high-order sliding-mode control strategy, and is at the same time able to estimate the combination of known and unknown perturbations acting on the system. The disturbances d_h and d_V, coming from multiple uncertainties, are reconstructed online by only using the measurements provided by the navigation subsystem. Moreover, the scheme provides accurate estimates of the state derivatives, without the need to design a further differentiator.

The approach can be implemented by using a step-size, which is in the range of the nowadays on-board computers, and therefore significantly relaxes the corresponding computational requirements. Results show the feasibility of the approach, together with a significant improvement in the response of the system, especially in terms of transient, with respect to standard sliding-mode control strategies. The transient behavior improvement translates into a significantly smaller number of violations of the maximum value of constraints, in this specific case the load factor, and in general to an improvement of the final errors. Moreover, the estimates match very well with the

true derivatives and disturbances, confirming the validity of the proposed adaptive approach.

Appendix

The terms a_h, a_V, $b_{h,\alpha}$, $b_{h,\mu}$, $b_{V,\alpha}$, $b_{V,\mu}$ can be computed as follows.

$$a_h = 2\dot{V}\dot{\gamma}\cos\gamma - V\dot{\gamma}^2\sin\gamma + \sin\gamma a_V + V\cos\gamma a_\gamma \tag{53}$$

$$a_V = -a_D - g_h\sin\gamma\dot{h} - g\cos\gamma\dot{\gamma} \tag{54}$$

$$b_{h,\alpha} = \sin\gamma b_{V,\alpha} + V\cos\gamma b_{\gamma,\alpha} \tag{55}$$

$$b_{h,\mu} = V\cos\gamma b_{\gamma,\mu} \tag{56}$$

$$b_{V,\alpha} = -b_{D,\alpha} \tag{57}$$

$$b_{V,\mu} = 0 \tag{58}$$

$$a_D = D\left(\frac{\rho_h}{\rho} + \frac{C_{D,h}}{C_D}\right)\dot{h} + D\left(\frac{2}{V} + \frac{C_{D,M}M_V}{C_D}\right)\dot{V} + D\left(\frac{C_{D,\alpha}}{C_D}\right)\dot{\alpha}_{\text{ref}} \tag{59}$$

$$a_L = L\left(\frac{\rho_h}{\rho} + \frac{C_{L,h}}{C_L}\right)\dot{h} + L\left(\frac{2}{V} + \frac{C_{L,M}M_V}{C_L}\right)\dot{V} + L\left(\frac{C_{L,\alpha}}{C_L}\right)\dot{\alpha}_{\text{ref}} \tag{60}$$

$$b_{D,\alpha} = D\frac{C_{D,\alpha}}{C_D} \tag{61}$$

$$b_{L,\alpha} = L\frac{C_{L,\alpha}}{C_L} \tag{62}$$

$$a_\gamma = \left(\frac{1}{r} + \frac{g}{V^2}\right)\dot{V} - \left(\frac{V}{r^2} + \frac{g_h}{V}\right)\dot{h}\cos\gamma - \frac{L}{V^2}\dot{V}\cos\mu - \frac{L}{V^2}\sin\mu\dot{\mu}_{\text{ref}} \tag{63}$$

$$- \dot{\gamma}\left(\frac{V}{r} - \frac{g}{V}\right)\sin\gamma + \frac{a_L}{V}\cos\mu \tag{64}$$

$$b_{\gamma,\alpha} = \frac{b_L}{V}\cos\mu \tag{65}$$

$$b_{\gamma,\mu} = -\frac{L}{V}\sin\mu \tag{66}$$

Moreover, the partial derivatives of Mach number with respect to the altitude h and the velocity modulus V are computed as follows,

$$\begin{aligned} M_h &= -\frac{M}{2}\frac{T_h}{T} \\ M_V &= \frac{1}{\sqrt{\gamma_{gas}R_{gas}T}} \end{aligned} \tag{67}$$

with T_h representing the derivative of the atmospheric temperature T with respect to h, and computed numerically. γ_{gas} is the air specific heat ratio, equal to 1.4, and R_{gas} is the specific gas constant, assumed equal to 287.05 J / (kg K).

References

[1] Bogner I., "Description of Apollo Entry Guidance," NASA TM CR-110924, 1966.

[2] Tu K. Y., Munir M. S., Mease, K. D. and Bayard D. "Drag-Based Predictive Tracking Guidance for Mars Precision Landing," *Journal of Guidance, Control and Dynamics*, Vol.23 No. 4, July-August 2000, pp.620-628, doi:10.2514/2.4607.

[3] Benito J. and Mease, K. D., "Reachable and Controllable Sets for Planetary Entry and Landing," *Journal of Guidance, Control and Dynamics*, Vol.33 No. 3, pp.641-654, doi:10.2514/1.47577.

[4] Ross I. M., "A Beginner's Guide to DIDO, ver 7.3, A Matlab Application Package for Solving Optimal Control Problems", *Document # TR-711*, Elissar, LLC, 2014.

[5] Bollino K. P., "High-Fidelity Real-Time Trajectory Optimization for Reusable Launch Vehicles", Ph.D. Dissertation, Mechanical and Astronautical Engineering Dept., Naval PostGraduate School., 2006.

[6] Sagliano M. and Theil S., "Hybrid Jacobian Computation for Fast Optimal Trajectories Generation", *AIAA Guidance, Navigation, and Control (GNC) Conference*, AIAA 2013-4554, Boston, MA, 2013, doi:10.2514/6.2013-4554

[7] Huneker, L., Sagliano M. and Arslantas Y.E., "SPARTAN: An Improved Global Pseudospectral Algorithm for High-Fidelity Entry-Descent-Landing Guidance Analysis, "*30^{th} International Symposium on Space Technology and Science*, Kobe, Japan, 2015.

[8] Gill, P. E., Murray W. and Saunders M. A., "User's Guide for SNOPT Version 7: Software for Large-Scale Nonlinear Programming"', Software User Manual, Department of Mathematics, University of California, San Diego, CA, 2008

[9] Wächter A. and Biegler L.T., "On the implementation of an interior-point filter linesearch algorithm for large-scale nonlinear programming", *Math. Program. 106(1)*, Springer-Verlag, New York, 2006.

[10] Harpold, J. C. and Graves, C. A., Jr., "Shuttle Entry Guidance," *Journal of the Astronautical Sciences*, Vol. 27, No. 3, 1979, pp. 239-268.

[11] Mease K. D. and Kremer J.P, "Shuttle Entry Guidance Revisited Using Nonlinear Geometric Methods", *Journal of Guidance, Control and Dynamics*, Vol.17 No. 6, 1994, pp.1350-1356, doi:10.2514/3.21355.

[12] Bharadwaj S., Rao A. V. and Mease, K. D., "Entry Trajectory Law via Feedback Linearization",*Journal of Guidance, Control and Dynamics*, Vol.21 No. 5, 1998, pp.726-732, doi:10.2514/2.4318.

[13] Saraf A., Levitt J.A., Mease K.D. and Ferch M., AIAA-2004-4774, "Landing footprint computation for entry vehicles," *AIAA Guidance, Navigation and Control Conference and Exhibit*, Providence, RI, 2004, doi:10.2514/6.2004-4774.

[14] Lu P. and Hanson J. M., "Entry Guidance for the X-33 Vehicle,"*Journal of Spacecraft and Rockets*,

Vol.35 No. 3, 1998, pp.342-349, doi:10.2514/2.3332.

[15] Lu P., "Regulation About Time-Varying Trajectories: Precision Entry Guidance Illustrated,"*Journal of Guidance, Control and Dynamics*, Vol.22 No. 6, 1999, pp.784-790, doi:10.2514/2.4479.

[16] Lu P., "Entry Guidance: A Unified Method ,"*Journal of Guidance, Control and Dynamics*, Vol.37 No. 3, May-June 2014, pp.713-728, doi:10.2514/1.62605.

[17] Roenneke A. J. and Cornwell P. J., "Trajectory Control for a Low-Lift Entry Vehicle," *Journal of Guidance, Control and Dynamics*, Vol.16 No. 5, September-October 1993, pp.927-933, doi:10.2514/3.21103.

[18] Roenneke A. J. and Markl A., "Reentry Control to a Drag Vs. Energy Profile," *Journal of Guidance, Control and Dynamics*, Vol.17 No. 5, September-October 1994, pp.916-920, doi:10.2514/3.21290.

[19] Mooij E.: "Model Reference Adaptive Guidance for Re-entry Trajectory Tracking," *AIAA Guidance, Navigation, and Control Conference and Exhibit*, AIAA 2004-4775, Providence, RI, 2004, doi:10.2514/6.2004-4775.

[20] Mooij E.: "Robustness Analysis of an Adaptive Re-entry Guidance System," *AIAA Guidance, Navigation, and Control Conference and Exhibit*, AIAA 2005-6146, San Francisco, CA, 2005, doi:10.2514/6.2005-6146.

[21] Mooij E.: "Heat-Flux Tracking for Thermal-Protection System Testing," *AIAA/AAS Astrodynamics Specialist Conference*, AIAA 2014-4141, San Diego, CA, 2014, doi:10.2014/6.2014-4141.

[22] Mooij E.: "Adaptive Heat-Flux Tracking for Re-entry Guidance," *AIAA/AAS Astrodynamics Specialist Conference*, AIAA 2014-4144, San Diego, CA, 2014, doi:10.2014/6.2014-4142.

[23] Shtessel Y. B. and Shkolnikov I. A., "Aeronautical and Space Vehicle Control in Dynamic Sliding Manifolds," *International Journal of Control*, Vol.76 No. 9/10 2003, pp.1000-1017, doi:10.1080/0020717031000099065.

[24] Harl N. and Balakrishnan S. N., "Reentry Terminal Guidance Through Sliding Mode Control," *Journal of Guidance, Control and Dynamics*, Vol.33 No. 1, July-August 2000, pp.186-199, doi:10.2514/1.42654.

[25] Furfaro R. and Wibben D. R., "Mars Atmospheric Entry Guidance via Multiple Sliding Surface Guidance for Reference Trajectory Tracking," *AIAA/AAS Astrodynamics Specialist Conference*, AIAA 2012-4435, Boston, MA, doi:10.2514/6.2012-4435.

[26] Utkin V. I., and Poznyak A. S., *Adaptive Sliding Mode Control with Application to Super-Twisting Control: Equivalent Control Method, Automatica*, Vol.49, pp.39-47, doi:*Automatica*, Vol.49, pp.183-190, doi:10.1016/j.automatica.2015.11.038.

[27] Yu P., Shtessel Y., and Edwards C., *Adaptive Continuous Higher ORder Sliding Mode Control of Air Breathing Hypersonic Missile for Maximum Penetration, AIAA Guidance, Navigation, and Control*

(GNC) Conference, AIAA 2015-2003, Kissemmee, FL, 2015, doi:10.2514/6.2015-2003.

[28] Edwards C., and Shtessel Y., *Adaptive Continuous Higher Order Sliding Mode Control*, *Automatica*, Vol.65, pp.183-190, doi:10.1016/j.automatica.2015.11.038.

[29] Bhat S. P., and Bernstein D. S., *Geometric Homogeneity with applications to finite-time stability*, *Math. Control Signals Systems*, Vol.17, 2005, pp.101-127, doi:10.1007/s00498-005-0151-x.

[30] Shtessel Y., Edwards C., Fridman L. and Levant A., *Sliding Mode Control and Observation*, Birkhäuser-Springer, ISBN-10: 0817648925, New York, 2013, chapters 2-5.

[31] Sagliano, M., Samaan M., Theil S. and Mooij E.: "SHEFEX-3 Optimal Feedback Entry Guidance," *AIAA SPACE 2014 Conference and Exposition*, AIAA 2014-4208, San Diego, CA, 2014, doi:10.2514/6.2014-4208.

[32] Sagliano M., Oehlschlägel T., Theil S. and Mooij E., "Real time adaptive feedforward guidance for entry vehicles", *3rd Ceas Eurognc conference*, Toulouse, 2015

[33] Sagliano. M., Mooij E. and Theil S., "Onboard Trajectory Generation for Entry Vehicles via Adaptive Multivariate Pseudospectral Interpolation", *Journal of Guidance, Control and Dynamics*, 2016, doi: 10.2514/1.G001817

[34] Sagliano M.,"Development of a Novel Algorithm for High Performance Reentry Guidance", *Ph.D. Dissertation*, Fachbereich Produktionstechnik , University of Bremen, 2016

[35] Weihs. H., "The SHEFEX Story: A Historical Review 2001-2014", *5th International ARA Days*, Avantage-Aquitaine, 2015

[36] Jiang, L., Wu Q. H., "Nonlinear Adaptive Control via Sliding-Mode State and Perturbation Observer",*Control Theory Applications, IEE Proceedings*, Vol. 149, No. 4, July 2002, pp.269-277, doi:10.1049/ip-cta:20020470.

[37] Talole, S. E., Benito J., Mease K. D., "Sliding Mode Observer for Drag Tracking in Entry Guidance",*AIAA Guidance, Navigation, and Control (GNC) Conference and Exhibit*, AIAA 2007-6851, Hilton Head, SC, 2007, doi:10.2514/6.2007-6851.

[38] Steffes S. R., "Development and Analysis of SHEFEX-2 Hybrid Navigation System Experiment," Fachbereich Produktionstechnik, Universität Bremen, Bremen, Germany, 2012.

[39] Xu H., Mirmirani M. D. and Ioannou P. A., "Adaptive Sliding Mode Control Design for a Hypersonic Flight Vehicle",*Journal of Guidance, Control and Dynamics*, Vol.27 No. 5, September-October 2004, pp.829-838, doi:10.2514/1.12596.

[40] Mooij, E., *Linear Quadratic Regulator Design for an Unpowered, Winged Re-entry Vehicle*, Series 08 - Astrodynamics and Satellite Systems , No. 3, Delft University Press, Delft, 1998.

[41] Mooij, E., "Passivity Analysis for Non-Linear, Non-Stationary Entry Capsules: Translational Motion", *International Journal of Adaptive Control and Signal Processing, Special Issue: Simple and Robust Adaptive Control*, Vol. 28, No.7-8, July-August 2014, pp.708-731, doi:10.1002/acs.2386.

[42] Mooij E., "Characteristic Motion of Re-entry Vehicles", AIAA Atmospheric Flight Mechanics (AFM) Conference, AIAA 2013-4603, Boston, MA, 2005, doi:10-2514/6.2013-4603.

[43] Neeb D., and Gülhan A., "Experimentelle Bestimmung der aerodynamischen Beiwerte von SHEFEX II im H2K", *DLR Technical Report IB-32418âĂŞ2009A36*, 2012.

[44] ESA, "Margin Philosophy for Science Assessment Studies", *ESA Technical Report SRE-PA/2011.097*, 2012.